A&A, 714, A84 (2026)
https://doi.org/10.1051/0004-6361/202558566
© The Authors 2026

Astronomy & Astrophysics

Alfvénic solar wind intervals observed by Solar Orbiter: Exploiting the capability of the SWA plasma suite and source region investigation

R. D'Amicis[1,⋆], J. M. Raines[2], S. Benella[1], O. Panasenco[3], M. Velli[4], G. Nicolaou[5], C. J. Owen[5], R. M. Dewey[2], P. Louarn[6], A. Fedorov[6], S. T. Lepri[2], B. L. Alterman[7], D. Perrone[8], R. De Marco[1], R. Bruno[1], L. Sorriso-Valvo[9,10], O. S. Dhamane[1], Y. Rivera[11], O. R. Kieokaew[6], D. Verscharen[5], G. Consolini[1], S. Yardley[12], V. Réville[6], D. Telloni[13], D. Baker[5], G. Lewis[5], G. Watson[5], C. Anekallu[5], K. Darwish[5], L. Prech[14], S. Livi[15], T. Horbury[16], G. Mele[17], V. Fortunato[18], and F. Monti[19]

[1] Institute for National Astrophysics (INAF), Institute for Space Astrophysics and Planetology (IAPS), Via del Fosso del Cavaliere, 100, 00133 Rome, Italy
[2] Department of Climate and Space Sciences and Engineering, The University of Michigan, Ann Arbor, MI, 48109, USA
[3] Advanced Heliophysics, Pasadena, USA
[4] Department of Earth, Planetary, and Space Sciences, University of California, Los Angeles, CA, 90095, USA
[5] University College London, Mullard Space Science Laboratory, Holmbury St. Mary, Dorking, Surrey, RH5 6NT, UK
[6] Institut de Recherche en Astrophysique et Planétologie, CNRS, Université de Toulouse, CNES, Toulouse, France
[7] Heliophysics Science Division, NASA Goddard Space Flight Center, Greenbelt, MD, USA
[8] ASI - Italian Space Agency, Rome, Italy
[9] CNR - National research Council, ISTP - Institute for Plasmas Science and Technology, Bari, Italy
[10] KTH Royal Institute of Technology, School of Electrical Engineering and Computer Science, Department of Electromagnetics and Plasma Physics, Stockholm, Sweden
[11] Center for Astrophysics–Harvard & Smithsonian, 60 Garden Street, Cambridge, MA 02138, USA
[12] Department of Mathematics, Physics and Electrical Engineering, Northumbria University, Newcastle Upon Tyne, UK
[13] Institute for National Astrophysics (INAF) - Osservatorio Astrofisico di Torino, Torino, Italy
[14] Faculty of Mathematics and Physics, Charles University, Prague, Czech Republich
[15] Southwest Research Institute, 6220 Culebra Road, San Antonio TX, 78238, USA
[16] Department of Physics, Imperial College London, London, UK
[17] LEONARDO SpA, Grottaglie, 74023 Taranto, Italy
[18] Planetek Italia S.R.L., Via Massaua, 12, 70132 Bari, BA, Italy
[19] TSD-Space, Via San Donato 23 - 80126 Napoli, Italy

Received 14 December 2025 / Accepted 3 June 2026

ABSTRACT

Context. Fast and slow solar wind have distinct properties linked to their solar sources. The Alfvénic slow wind complicates the usual classification by solar-wind speed, especially at intermediate speeds. The Solar Wind Analyzer (SWA) on Solar Orbiter offers unique capabilities to investigate how Alfvénic slow wind differs from classical fast wind, and relates these differences to their solar origins.
Aims. In September 2022, Solar Orbiter moved inbound toward the Sun from 0.59 to 0.38 AU, and observed several Alfvénic streams: one fast wind (F), three Alfvénic slow wind intervals (AS1, AS2, AS3), and a moderate fast wind (MF); a non-Alfvénic slow wind (S) interval was included for comparison. We analyzed these streams to highlight their similarities and differences.
Methods. We combined plasma parameters from all SWA sensors with magnetic field measurements from the magnetometer (MAG). A spectral analysis of magnetic and velocity fluctuations was used to characterize the Alfvénicity. The magnetic connectivity of each stream to its solar source was examined using potential field source surface extrapolation combined with ballistic backmapping from the spacecraft.
Results. Proton velocity distribution functions exhibit anisotropies and field-aligned beams typical of Alfvénic streams, while electron strahl populations become progressively broader and weaker from fast to non-Alfvénic slow wind. Heavy-ion composition shows a similarly ordered transition, where the Alfvénic slow wind displays intermediate charge-state ratios between fast and non-Alfvénic slow wind. Magnetic connectivity analysis associates the fast wind with a large coronal hole, whereas the Alfvénic slow wind intervals connect to open-field regions near pseudostreamers and overexpanded coronal-hole boundaries. Spectral analysis indicates that most Alfvénic streams remain close to energy equipartition despite their different heliocentric distances and bulk speeds. Altogether, these results support the interpretation of Alfvénic slow wind as the low-speed extension of coronal-hole-associated Alfvénic plasma undergoing a distinct acceleration and transport history.
Conclusions. The combined SWA observations offer key insights into how turbulence, particle transport, and coronal source conditions jointly shape the evolution of Alfvénic solar wind streams, revealing a coherent transition between fast, Alfvénic slow, and non-Alfvénic slow wind regimes.

Key words. turbulence – methods: data analysis – Sun: general – Sun: heliosphere – solar wind

⋆ Corresponding author: raffaella.damicis@inaf.it

Open Access article, published by EDP Sciences, under the terms of the Creative Commons Attribution License (https://creativecommons.org/licenses/by/4.0), which permits unrestricted use, distribution, and reproduction in any medium, provided the original work is properly cited.
This article is published in open access under the Subscribe to Open model. Subscribe to A&A to support open access publication.

1. Introduction

The solar wind is the classical paradigm of a collisionless plasma and a natural laboratory to study fundamental processes in astrophysical plasmas, including turbulence, magnetic reconnection, wave-particle interactions, and plasma instabilities (e.g., Verscharen et al. 2019a, and references therein). It is mainly composed of protons and electrons, with a few percent by number of alpha particles (fully ionized helium atoms, He^{2+}), and much less abundant heavy ions in different ionization stages (e.g., O^{6+}, C^{5+}, Fe^{9+}).

In situ measurements collected by various spacecraft over the last six decades have provided a detailed description of the solar wind over a wide range of distances from the Sun (e.g., Marsch et al. 1982a,b; Richardson et al. 2004; Raouafi et al. 2023), essentially from the corona to the heliopause (Maruca et al. 2023; Brown et al. 2025), and also covering a wide range of heliospheric latitudes (Bruno et al. 1986; Schwenn 1990; McComas et al. 1998, 2003; Elliott et al. 2003) and longitudes (Schwenn 1990). Such observations have shown the need to categorize the solar wind measurements according to different criteria in order to understand the origin of the wind, as well as its behavior and impacts in the heliosphere. The traditional classification based on the bulk speed, in which solar wind streams are generally separated into two distinct "states", fast and slow, is based on the bimodal distribution of speeds observed near Earth during solar minima (e.g., Bavassano & Bruno 1991). However, this classification is known to be imprecise, especially in the 400 to 600 km s^{-1} range of speeds and during different phases of solar activity (Schwenn 2006; D'Amicis et al. 2011; Fu et al. 2018; Alterman 2025).

The fast solar wind is typically associated with speeds exceeding 600 km s^{-1}, and is characterized by proton temperatures (T_p) that far exceed electron temperatures (T_e) in the inner corona, and at least up to 10 R_S from the Sun. At 1 AU, T_p is typically $\sim 2.3 \times 10^5$ K, while T_e is $\sim 1.0 \times 10^5$ K (e.g, Schwenn 1990). On the other hand, the near-ecliptic slow solar wind has distinct properties: its speed is typically <500 km s^{-1}, and the proton temperature tends to be lower than the electron temperature. The characteristics of the slow solar wind are far more variable than those of the fast solar wind (e.g., Schwenn 1990; Marsch et al. 1982b).

In general, the cause of their different properties can be traced back to their different solar sources. While the fast wind originates primarily from coronal holes, the slow solar wind is generally found close to the heliospheric current sheet, originating from closed magnetic field regions that intermittently open into the interplanetary medium, most likely due to reconnection processes, or from high flux tube expansion. However, the sources of the slow solar wind are still a matter of debate (e.g., Wang & Sheeley 1990; Noci et al. 1997; Ofman 2000; Antonucci et al. 2005; Antiochos et al. 2011; Abbo et al. 2016). During the minima of solar activity, the slow wind is usually observed close to the heliospheric current sheet (Smith et al. 1978; Bavassano et al. 1997), while during maxima, because of the more complex structure of the solar corona (McComas et al. 2001), it is generally associated with the presence of streamers (Wang et al. 1999) and low-latitude small coronal holes (e.g., Wang 1994).

Fast and slow solar wind streams differ significantly in the local microphysics governing the thermodynamic properties and relative streaming of the main particle populations. Proton velocity distribution functions (VDFs) in fast wind are typically characterized by large temperature anisotropies, with the perpendicular temperature component larger than the parallel one ($T_\perp > T_\parallel$) with respect to the magnetic field direction, especially close to the Sun, and by the presence of proton beam populations drifting along the magnetic field with velocities on the order of the local Alfvén speed or higher (Feldman et al. 1973; Marsch et al. 1982b; Goldstein et al. 2000; Alterman et al. 2018). In contrast, slow wind proton VDFs are generally more isotropic and exhibit weaker or absent beam components (Marsch et al. 1982b; Hellinger et al. 2006; Matteini et al. 2013; Alterman et al. 2018).

Alpha particles represent the second most abundant ion population, accounting for up to 20% of the solar wind mass density. They also display substantial differences between the two wind regimes. Fast wind is typically associated with enhanced alpha abundance, significant proton–alpha differential streaming, and the presence of massive alpha beams, whereas slow wind exhibits lower alpha abundance, weaker differential streaming, and more nearly thermal equilibrium between proton and alpha populations (Neugebauer & Snyder 1962; Marsch et al. 1982a; Kasper et al. 2008; Maruca et al. 2013; Alterman et al. 2018; Bruno et al. 2024; Alterman & D'Amicis 2025a,b). These kinetic differences are generally interpreted as signatures of different source-region conditions and distinct transport and wave-particle interaction histories during solar wind expansion.

Electron VDFs consist of three distinct populations as observed in earlier missions: Helios (Feldman et al. 1975; Pilipp et al. 1987a,b); Ulysses (Hammond et al. 1996; Maksimovic et al. 1997), and Wind (Fitzenreiter et al. 1998; Salem et al. 2023). They consist of a thermal core, well described by a Maxwellian distribution with thermal energy of ~10 eV; a non-thermal halo, mostly following a κ-distribution that captures the enhanced high-energy tails, with thermal energy <80 eV; and a strahl, with bulk energy ≤100 eV. While the core and halo populations are generally relatively isotropic, the strahl is a strongly field-aligned (or anti-aligned) beam of electrons, typically traveling antisunward, due to its large drift along the field, that can cause a large anisotropy in the overall VDFs (e.g., Feldman et al. 1978; Pilipp et al. 1987a). The strahl is found to be narrow and highly collimated in fast solar wind streams, while it becomes broader, or absent (or fully isotropized) in examples of slower winds (Pilipp et al. 1987a). Bidirectional strahl events, when present, are often associated with newly closed magnetic loops or suprathermal electrons reflected at interplanetary shocks (e.g., Gosling et al. 1987; Owens & Forsyth 2013), and are commonly observed in association with coronal mass ejections at 1 AU (e.g., Gosling et al. 1987). Understanding unidirectional and bidirectional strahl trajectories, through the analysis of electron pitch angle distributions (PADs), can help determine large-scale interplanetary magnetic field (IMF) topology and provide indications of solar connectivity (e.g., Pilipp et al. 1987b; Owens & Forsyth 2013). The strahl likely originates as a more isotropic distribution of electrons in the corona that is focused by the mirror effect as these escaping electrons propagate outward along the weakening magnetic field in the nascent solar wind (e.g., Owens et al. 2008). This may explain the antisunward bulk velocity of the strahl that is usually observed in the solar-wind rest frame. However, as for the ion beams, a Sunward or bidirectional electron strahl can occur when the magnetic-field configuration changes during the plasma expansion from the Sun (e.g., Gosling et al. 1987; Owens et al. 2017). Pitch angle scattering of the strahl has also been suggested as a potential source of the more isotropic halo (e.g., Vocks et al. 2005; Saito & Gary 2007; Verscharen et al. 2019b).

Heavy ions have been shown to be tracers of physical processes in the solar wind and provide crucial information about

the origin and the evolutionary processes of the solar wind from the corona into the heliosphere (e.g., Raymond et al. 1997; von Steiger et al. 2000; Zurbuchen 2007). Elemental abundance ratios are powerful indicators of solar wind source regions on the Sun (von Steiger et al. 2000). The ionic charge state distributions (the relative abundance of each charge state for a given element compared to the total element abundance) observed in situ are determined by the temperature, density, and expansion profiles in the inner corona, where a solar wind parcel originates (Geiss et al. 1995a). As a solar wind parcel expands while moving outward from the Sun, these heavy ion charge state distributions are frozen at the values they have in the low corona, so that measurements beyond this point reveal the temperature of the corona at the origin of the parcel. Charge state ratios are simplified indicators of this, computed from pairs of charge states. The most common are O^{7+}/O^{6+} and C^{6+}/C^{5+}. The in situ elemental abundances in the two solar wind regimes also show clear differences: in slow speed wind, heavy elements have low first ionization potential (FIP $\leq$ 10 eV, i.e., low-FIP elements) and are typically enhanced by a factor of 3–4 relative to the photosphere, a result of their containment on closed magnetic structures in the corona, while in the fast wind their abundances are more nearly photospheric (Geiss et al. 1995a; von Steiger et al. 2000; Zurbuchen et al. 1999). In addition, in the slow solar wind the freeze-in temperature determined from carbon charge states is 1.4–1.6 $\times$ 10^6 K, while in the fast wind it is 8 $\times 10^5$ K (e.g., Feldman et al. 2005). While the compositional information remains unchanged after the solar wind escapes the inner corona, the kinetic properties of heavy ions are strongly affected by local processes in the heliosphere (Isenberg & Hollweg 1983; Gary et al. 2001). For example, wave-particle interactions may result in nonthermal distributions of heavy ions. A preferential heating zone, extending to the Alfvén radius, nominally ~15 R_S, has been shown to act both on alpha particles (Kasper et al. 2017; Kasper & Klein 2019) and heavy ions (Holmes et al. 2024). Beyond this zone, Coulomb collisions tend to push particles toward thermal equilibrium in the solar wind rest frame (Maruca et al. 2013; Johnson et al. 2024). Although heavy ions also transition toward thermal equilibrium, their behavior is more nuanced (Tracy et al. 2015, 2016; Holmes et al. 2024) and radial evolution may need to be accounted for (Rivera, et al. 2025b).

While fast and slow solar wind streams differ in several kinetic and compositional properties, they also exhibit markedly different levels of Alfvénicity. Fast wind is typically characterized by large-amplitude mainly outward-propagating Alfvénic fluctuations, playing a fundamental role in the turbulent dynamics, whereas slow wind generally displays lower Alfvénicity together with a more compressive and variable character (Belcher & Davis 1971; Tu & Marsch 1995; Bruno & Carbone 2013). Alfvénic fluctuations are thought to play a major role, particularly through wave–particle interactions that shape nonthermal features such as temperature anisotropies, beams, and differential flows observed in ion VDFs. However, the distinction between fast and slow wind and their mapping to distinct source regions become less clear when solar wind composition and turbulence properties are taken into account (e.g., von Steiger 2008; Zhao et al. 2009, 2017; Stakhiv et al. 2015; Xu & Borovsky 2015; D'Amicis & Bruno 2015; Camporeale et al. 2017; Ko et al. 2018; Stansby et al. 2018; Perrone et al. 2020; Alterman 2025; Alterman & D'Amicis 2025a; Alterman et al. 2025a,b; Alterman & D'Amicis 2025b).

The Alfvénic slow wind (AS, D'Amicis et al. 2011; D'Amicis & Bruno 2015) is an emerging class of solar wind characterized by slow wind-like bulk speeds, and by several properties more commonly associated with fast wind streams. This regime is referred to as Alfvénic slow wind because the Alfvénic nature of the fluctuations represents one of its defining properties. Examples of Alfvénic slow wind have been extensively investigated in terms of their compositional, thermodynamic, kinetic, and turbulent properties (D'Amicis et al. 2011; D'Amicis & Bruno 2015; D'Amicis et al. 2019, 2020; Stansby et al. 2020; Perrone et al. 2020; D'Amicis et al. 2021a), revealing several similarities with fast streams, including similar coronal source environments. In particular, several studies have pointed out the relationship between the Alfvénic slow wind and rapidly expanding low-latitude coronal holes (e.g., Wang 1994; Wang et al. 2012; Panasenco & Velli 2013) in the presence of pseudostreamers (Panasenco et al. 2019, 2020; D'Amicis et al. 2021b). In this context, the different levels of Alfvénicity observed in fast, Alfvénic slow, and typical slow wind may reflect the differences in their coronal source regions (Yardley et al. 2024; Alterman & D'Amicis 2025a,b) and different evolution processes. Understanding how Alfvénicity relates to particle kinetics, composition, turbulence, and source-region properties is therefore essential in order to clarify the physical nature and origin of Alfvénic slow wind.

Addressing these questions requires simultaneous investigations of turbulence properties, particle kinetics, suprathermal electron populations, heavy-ion composition, and magnetic connectivity close to the Sun. Such a comprehensive approach is essential for disentangling the relative roles of coronal source conditions and interplanetary transport processes in shaping the observed solar wind properties. Before the launch of Parker Solar Probe (PSP) (Fox et al. 2016) only the two Helios spacecraft provided in situ observations of the inner heliosphere down to ~0.29 AU, enabling the first investigations of the radial evolution of solar wind plasma and turbulence properties (e.g., Tu & Marsch 1995). Subsequent missions at L1, such as ACE, Wind, DSCOVR, and more recently Aditya, significantly improved the long-term characterization of solar wind plasma and composition. In particular, the ACE mission provided the first continuous measurements of solar wind ionic composition and charge states, opening the possibility of systematically linking in situ plasma observations with coronal source conditions. Solar Orbiter (Müller et al. 2020) now provides a unique opportunity to investigate these processes through coordinated remote sensing and in situ observations obtained simultaneously in the inner heliosphere. In particular, the Solar Wind Analyzer (SWA) suite combines high-resolution proton and electron measurements with charge-resolved heavy-ion composition observations, enabling a comprehensive multi-sensor characterization of solar wind streams close to their source regions. When combined with magnetic connectivity analyses and remote sensing observations, these measurements provide unprecedented insight into the relationship between solar wind turbulence, kinetic properties, composition, and coronal origin.

The Solar Orbiter mission profile can be divided into three phases: cruise, nominal, and extended. After the Earth Gravity Assist Maneuver, which occurred on 26 November 2021, Solar Orbiter started its nominal mission, characterized by several close solar encounters at a heliocentric distance of around 0.3 AU. For this paper, we compared different Alfvénic streams observed during this phase of the mission, near the September 2022 perihelion, and identified the different constituents of the solar wind in each stream. We also compared and characterized the fluctuations of the different solar wind intervals to highlight the similarities and differences between them. We investigated their source regions and the properties that may drive these

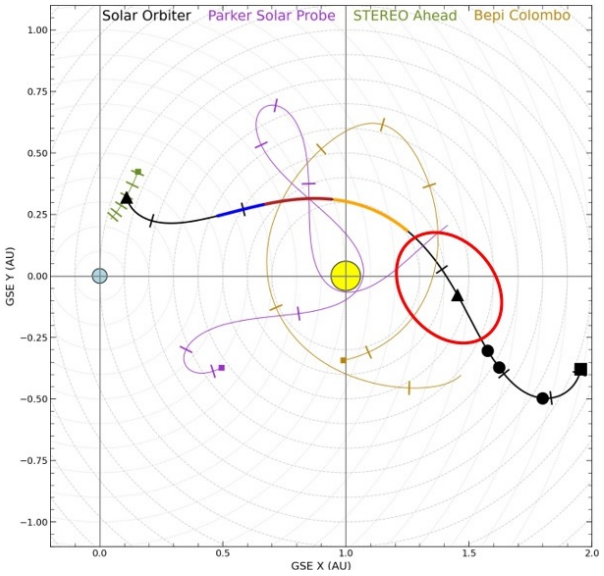


Fig. 1. Long-term planning (LTP) of Solar Orbiter operations 08 & 09 covering the time interval 27 June 2022–26 December 2022. The figure shows the X-Y projection of the Solar Orbiter orbit (solid black line) in GSE coordinates, along with PSP (purple), Stereo Ahead (green), and Bepi Colombo (yellow). The blue, red, and orange segments mark the remote sensing windows of Solar Orbiter. The black square indicates the period start, the triangles the LTP boundaries, and the black dots the GAM restrictions. The red oval highlights the interval investigated in this study (adapted from orbit plots available on the Solar Orbiter Confluence pages.).

different streams, showing how characterizing the Alfvénicity is critical for understanding these streams.

2. Observations overview

This paper analyzes several Alfvénic intervals observed by Solar Orbiter during the second half of September 2022, preceding the second perihelion passage of the nominal phase of the mission. Figure 1 illustrates the long-term planning (LTP) of Solar Orbiter operations (LTPs 08 & 09) covering the time interval 27 June 2022–26 December 2022. A fixed Earth-Sun reference frame is shown, using an X-Y projection of the orbit in GSE coordinates. The trajectory of Solar Orbiter is plotted as a solid black line. The figure also shows the trajectories of PSP (purple), STEREO Ahead (green), and Bepi Colombo (yellow). The blue, red, and orange segments along the Solar Orbiter path mark the length of the Solar Orbiter remote sensing windows, during which remote sensing observations are performed. The red oval highlights the interval investigated in the present study.

2.1. Instrument details

The plasma data were provided by the Solar Wind Analyzer (SWA) plasma suite (Owen et al. 2020). SWA consists of three sensors dedicated to fully characterize the solar wind: the Proton and Alpha particle Sensor (SWA-PAS), the Electron Analyzer System (SWA-EAS) and the Heavy Ion Sensor (SWA-HIS), served by a common Data Processing Unit (SWA-DPU).

SWA-PAS is a top-hat electrostatic analyzer that measures the 3D VDF of the solar wind ions (protons and alpha particles) without mass selection at 92 energies (logarithmically spaced from 200 eV/q to 20 keV/q), 11 azimuth (−24° to +42°) and 9 elevation (±22.5°) angles (with ∼6° × 6° angular resolution). The complete sweep over all energy steps and elevation angles is performed in 1 s and repeated with a cadence of 1 or 4 s. Level 2 (L2) SWA-PAS ground moments (i.e number density, velocity vector, and temperature from the pressure tensor trace) refer to protons only, obtained after removing alpha particles by cutting the 1-D distribution at the saddle point between the two populations.

SWA-EAS consists of two top-hat electrostatic analyzer heads, mounted orthogonally to each other at the end of a 4-m long boom extending into the shadow of the spacecraft. Each head has a field of view ∼90° × 360° (elevation × azimuth). Due to the orthogonal mounting of the 2 heads, SWA-EAS has a combined field of view that covers the full sky, with the exception of regions blocked by the spacecraft or its appendages. The instrument samples electrons within the energy range from ∼1 eV to ∼5 keV. The SWA-EAS measurements are used to resolve the 3D VDFs of thermal core, supra-thermal halo and strahl electrons. By combining the 3D VDFs from SWA-EAS with the magnetic field measurements by MAG, and assuming the distributions are gyrotropic, we constructed 2D pitch-angle versus energy distribution functions, with one reference axis being along the magnetic field (Owen et al. 2022). These distributions are convenient to visualize the electron beams, from which we can infer the topological nature of the observed magnetic structure (e.g., switchback, closed field loop) and its magnetic connection to the solar source.

SWA-HIS is a charge-resolving ion mass spectrometer which uses a top-hat electrostatic analyzer paired with a time-of-flight (TOF) telescope. Together they select ions by energy per charge (E/q) before measuring their TOF and total energy (E), allowing the separation of solar wind ions by both mass and charge (Owen et al. 2020). SWA-HIS scans its full range of E/q, 0.5 keV/q to 75 keV/q, every 30 seconds. These measurements are accumulated over 10 min for publicly released data products. During ground processing, these data pass through a maximum likelihood estimator (MLE) method to assign counts in the TOF-E measurement space to specific ions with minimal uncertainty due to overlap. This MLE method was first developed for ACE/SWICS (Shearer et al. 2014) and has been adapted for SWA-HIS (Livi et al. 2023) to derive ion densities, velocities, and thermal speeds. Charge state distributions, and ratios such as O^{7+}/O^{6+}, C^{6+}/C^{5+} and C^{6+}/C^{4+}, as well as the elemental abundance ratio Fe/O were derived from these SWA-HIS measurements and were used in this study.

The magnetic field measurements are provided by the magnetometer (MAG) instrument (Horbury et al. 2020a), averaged at SWA-PAS sampling time. The velocity and magnetic field data are given in the heliographic radial-tangential-normal (RTN) coordinate system, where R points away from the Sun toward the spacecraft, T is the cross product of the Sun's spin axis and R, and N completes the right-handed triad. The data from all instruments used in this study are available through the Solar Orbiter Archive[1].

2.2. Event overview and data selection

Figure 2 shows an overview of the whole interval of interest, from 14 September to 2 October, 2022, with the time series of the relevant parameters observed by Solar Orbiter. During this interval, the heliocentric distance of the spacecraft decreased from 0.58 to 0.38 AU. Figure 2 shows, from top to bottom: solar wind bulk speed, V_{sw} [km s^{-1}]; the heliocentric distance, R [AU]; the

[1] http://soar.esac.esa.int/

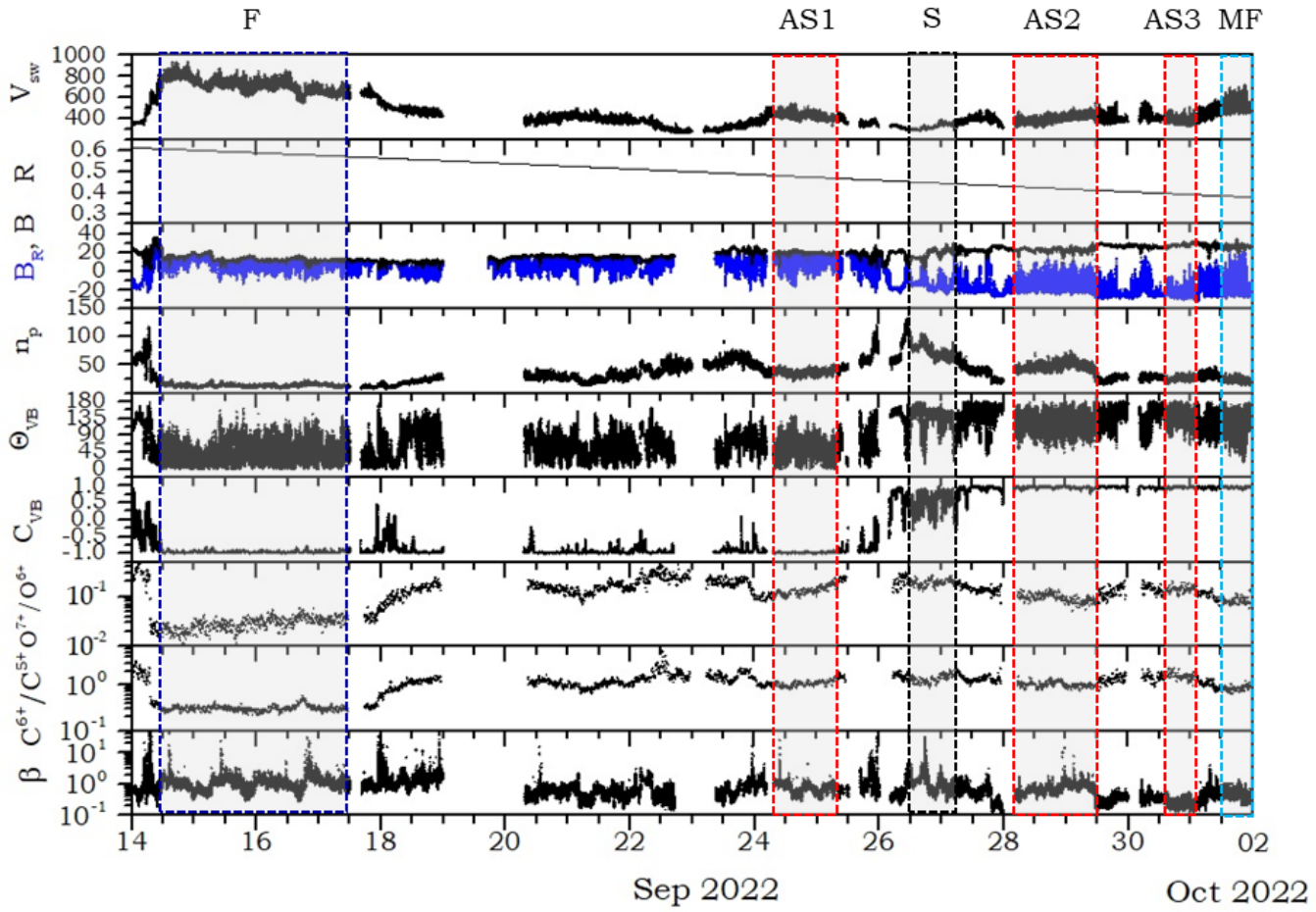


Fig. 2. Overview of time series of relevant solar wind parameters observed by Solar Orbiter at a heliocentric distance ranging between 0.58 and 0.32 AU. From top to bottom: solar wind bulk speed, V_{sw}, in km s^{-1}; heliocentric distance, R, in AU; radial component of the magnetic field, B_R, in nT (blue) and magnetic field magnitude, B, in nT (black); number density, n_p, in cm^{-3}; the angle the magnetic field forms with the velocity field, Θ_{BV}, in degrees; v-b correlation coefficient computed at 30 min scale using a running window, C_{VB}; the charge state O^{7+}/O^{6+} ratio; the charge state C^{6+}/C^{5+} ratio; plasma β. The colored boxes identify the intervals investigated in this study, corresponding to separate streams of fast wind (F), Alfvénic slow wind (AS1, AS2, AS3), moderate fast wind (MF), and non-Alfvénic slow (S) solar wind.

radial component of the magnetic field, B_R (blue), and magnetic field magnitude, B (black), [nT]; the proton number density, n_p [cm^{-3}]; the angle the magnetic field forms with the velocity vector, Θ_{VB} [degrees]; the correlation coefficient of velocity and magnetic field components, C_{VB}; the charge state O^{7+}/O^{6+} ratio; the charge state C^{6+}/C^{5+} ratio; the plasma β.

The parameter C_{VB} is the Pearson's correlation coefficient between V and B components, calculated separately for the three RTN components using a running window of 30 min length (e.g., Tu et al. 1989) and then averaged ($\sum_{i=R,T,N} C_{V_iB_i}/3$). The sign of correlation is given by $-sign(k \cdot B)$. Since the direction of the wavevector k cannot be directly determined from single-spacecraft measurements, this relation cannot be unambiguously evaluated. However, under the reasonable assumption that the fluctuations are predominantly outward propagating in the solar wind, the observed sign of the correlation is determined by the polarity of the magnetic field. If the magnetic field has a negative polarity ($B < 0$), the V and B components are correlated ($C_{VB} > 0$); instead, if the magnetic field polarity is positive, the V and B components are anticorrelated ($C_{VB} < 0$).

The time interval from 14 to 18 September, highlighted in Figure 2 by the gray shading labeled F, is dominated by a fast wind stream. The main portion of this stream is characterized by a bulk speed exceeding 600 km s^{-1}. The kinetic properties of protons and alpha particles of the fast stream were reported in detail by Bruno et al. (2024). This fast stream is followed by a rarefaction region, where the bulk speed drops to 400 km s^{-1}, and subsequently by a more standard non-Alfvénic slow wind (around 18 September) with C_{VB} approaching 0. The remaining part of the interval shown in Figure 2 is mainly characterized by slow wind streams. In general, the C_{VB} coefficient is negative (anticorrelated $V - B$ components) and high, with a well-defined magnetic field (inward) polarity, as in typical Alfvénic intervals. In contrast, just after 26 up to mid 27 September, a fluctuating C_{VB} passing from positive to negative values is observed, indicating the presence of more standard (non-Alfvénic) slow wind, although there are also other intervals where C_{VB} fluctuates and thus identifies non-Alfvénic solar wind (after 14, 18 and 24 September). The two solar wind regimes identified here are also characterized by different amplitudes in velocity and magnetic field fluctuations, which are seen to be larger in Alfvénic slow streams. In this particular case, only the B_R component is shown, but it is representative to show the amplitude of the fluctuations in the different streams. We must also take into account the dependence of Alfvénicity on radial distance. In this interval, the heliocentric distance decreases with time, which may

Table 1. Bulk parameters averaged over the selected intervals.

Interval	Begin	End	R [AU]	V_{sw} [km s^{-1}]	n_p [cm^{-3}]	T_p [10^5 K]	B [nT]
F	2022-09-14T14:24:00	2022-09-17T12:00:00	0.588	704.	13.3	4.08	13.6
AS1	2022-09-24T07:12:00	2022-09-25T08:24:00	0.474	424.	36.4	2.30	19.8
S	2022-09-26T12:00:00	2022-09-27T06:00:00	0.443	342.	66.3	1.59	20.4
AS2	2022-09-28T04:48:00	2022-09-29T10:48:00	0.419	395.	48.5	2.34	23.1
AS3	2022-09-30T12:00:00	2022-10-01T00:00:00	0.393	383.	25.7	2.14	27.0
MF	2022-10-01T12:00:00	2022-10-02T00:00:00	0.381	520.	23.2	4.09	26.6

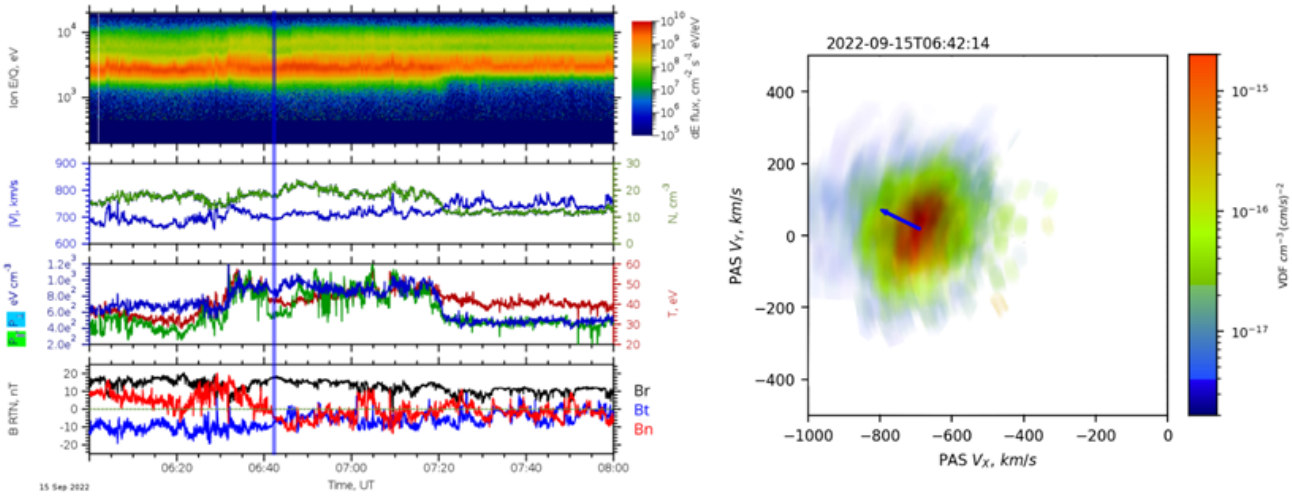


Fig. 3. SWA-PAS and MAG observations during the Fast solar wind interval. Left panel (from top to bottom): energy–time spectrogram of the ion energy differential flux; solar wind velocity (blue) and number density (green); parallel pressure $P_{\parallel}$ (green), perpendicular pressure $P_{\perp}$ (blue), and temperature T (red); and magnetic field vector components in RTN coordinates. The vertical blue line indicates the time of the VDF shown in the right panel. Right panel: ion velocity distribution function (VDF) in the $\mathbf{V} \times \mathbf{B}$ plane. The X-axis is aligned as closely as possible with the spacecraft–Sun direction. The blue arrow shows the magnetic field vector.

determine the larger amplitude of the fluctuations observed in the Alfvénic slow wind compared to the earlier fast wind. The analysis which follows in this paper is based on the comparison of a number of selected intervals identified by the shaded regions between the colored vertical dashed lines in Figure 2: AS1, AS2, and AS3 identify portions of Alfvénic slow wind with similar bulk speed (average speed 400 km/s); F is a fast wind interval and MF is an intermediate wind (MF stands for moderate fast). Table 1 shows the average bulk parameters for the selected intervals. The Alfvénic slow wind intervals are identified on the basis of high C_{VB} values, large-amplitude and weakly compressible fluctuations (indicated by almost constant magnetic field and number density). C_{VB} is however chosen only for the preliminary selection of the intervals. We investigate the full Alfvénic range of every stream in Section 4 by performing a spectral analysis.

During the interval of interest, we observe two heliospheric current sheet (HCS) crossings, one at the beginning of the interval and the other one just before 26 September. This allows us to identify two magnetic field polarities for the observed solar wind streams. The F and AS1 intervals are characterized by the same magnetic field (outward) polarity, while AS2, AS3 and MF by an opposite (inward) polarity. All intervals contain evidence for the presence of switchbacks, namely large and intermittent polarity reversals of the radial component of the magnetic field, (see Fig. 2) with amplitudes comparable to the magnitude of the magnetic field (Borovsky 2016; Bale et al. 2019). It should be noted that not only does the B_R component change sign within these structures, but the other components can also vary (Dudok De Wit et al. 2020). The occurrence and properties of switchback signatures change with heliocentric distance (e.g., Jagarlamudi et al. 2023).

3. Proton and alpha VDFs observed by SWA-PAS

SWA-PAS and MAG observations performed in the fast solar wind interval (15 September, 06:00–08:00 UT) and the AS1 interval (24 September, 14:00–16:00 UT) are presented in Figures 3 and 4, respectively. In both cases, an animated sequence showing the time evolution of the ion velocity distribution function (VDF) in the $\mathbf{V} \times \mathbf{B}$ plane is provided in the supplementary materials. The VDF images presented in these figures were generated using the direct volume rendering technique, commonly applied in computed tomography. The 3D VDF is treated as a transparent object, where the internal optical density and color are functions of the VDF value. Light rays are cast through the volume from behind, and color and opacity are accumulated along each ray to form the final 2D image. For further details, see Callahan et al. (2008).

For the fast wind (Figure 3), we selected, as an example, a time period during which the flow shows a transition between a perturbed state and a more stable one. In the energy

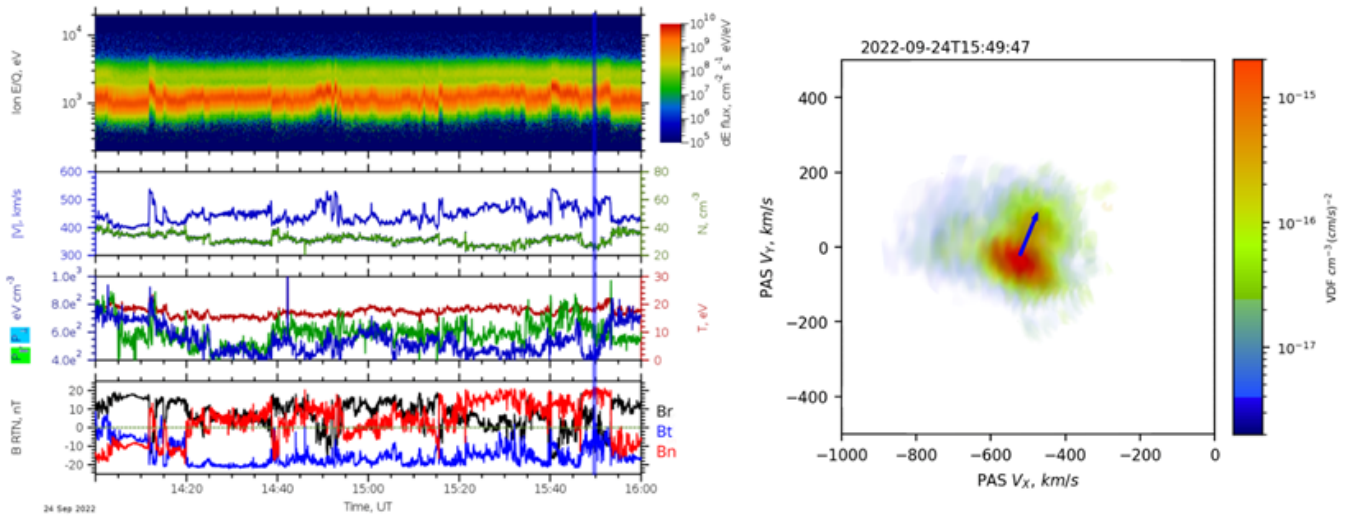


Fig. 4. Same as Figure 3, but for the slow solar wind case, corresponding to the time interval AS1 (see Figure 1).

spectrogram, the main proton population is observed at ~2.5–4.5 keV and the alpha particles appear as a yellow/green band, centered at 7–8 keV. Before 07:20 UT, the flow is perturbed, with density, velocity, temperature and pressure fluctuations of ~10–20% on timescales of a few 10 s. In particular, the pressure anisotropy ($P_\perp/P_\parallel$) abruptly varies from 1 to 2 and vice versa over timescales of a few seconds. After 07:20 UT, the flow is more stable. It slightly accelerates (from ~700–750 km s^{-1}), decreases in density (~20–12 cm^{-3}), and becomes almost isotropic ($P_\perp \sim P_\parallel$).

For the slow Alfvénic wind (Figure 4), the selected period is representative of the characteristic high level of turbulence of the flow. A key aspect is the almost perfect correlation between the magnetic and velocity fluctuations, consistent with the highly Alfvénic nature of the interval. The magnetic field is constant in magnitude, so its fluctuations are simply fast rotations that almost perfectly correlate with strong variations (up to ~100 km s^{-1}) seen in any component of the velocity.

SWA-PAS characteristic ion velocity distribution functions (VDFs) corresponding to each type of solar wind shown in Figure 2 are presented in Figure 5. In particular, 2D distributions integrated in the plane perpendicular to the $\mathbf{V} \times \mathbf{B}$ vector and including the solar wind bulk velocity vector are shown in the upper panels. In the bottom row, the $V_\parallel$ cut of each VDF is displayed. The fast 2D VFD displays a typical anisotropic distribution, characterized by $P_\perp \geq P_\parallel$. These VDFs can be described as classical bi-Maxwellian distributions. Their dominant anisotropic core appears as the red oval. A small secondary population (proton beam) is also observed along the magnetic field direction. The core and proton beam populations are shown in more detail in the $V_\parallel$ profiles. The proton beam is located approximately 150–250 km s^{-1} from the main peak, which is about twice the local Alfvén speed (~100 km s^{-1}). This is in agreement with Bruno et al. (2024) who studied the kinetic features of the different ion populations of the same fast wind. Moreover, a similar result was found by D'Amicis et al. (2025a) for another fast wind interval with Solar Orbiter data. Overall, this result is in agreement with previous studies using data from past missions (Feldman et al. 1973; Marsch et al. 1982b; Marsch and Livi 1987; Goldstein et al. 2000). For this particular case, the proton beam represents less than 5% of the total ion population. This estimate is again in agreement with Bruno et al. (2024) and with previous studies (Neugebauer & Snyder 1962, 1966; Asbridge et al. 1974; Yermolaev & Stupin 1997; Kasper et al. 2007). In the cases presented here, since the magnetic field is not aligned with the bulk flow, alpha particles are only marginally captured in the direction parallel to B. The secondary population observed in all $V_\parallel$ profiles of figure 2 is predominantly composed of protons.

The MF (moderate fast wind) VDFs, although anisotropic, differ from classical bi-Maxwellians due to their extended tails aligned with B. Their $V_\parallel$ profiles deviate from a Gaussian shape, instead appearing triangular when plotted on a logarithmic scale. This is a characteristic feature of hyperbolic distributions. As discussed in Louarn et al. (2024), this type of proton distribution, for which it is difficult to clearly distinguish a beam from the core, is not uncommon. Louarn et al. (2024) proposed to directly fit them by a skewed distribution, as the Normal Inverse Gaussian (NIG), introduced by Barndorff-Nielsen (1997) and now widely applied in various fields, such as finance, turbulence, biology, and technical modeling.

All AS distributions show a well-developed beam component, corresponding to nearly 30% of the main proton peak. The beam is located at ~120 km s^{-1} from the core population, which is about 1.6 the Alfvén velocity in the present case. This is in agreement with a recent study by D'Amicis et al. (2025a) that compared the drift speed of the proton beam of different Alfvénic slow wind intervals. In many cases, the gaussian fit of the core distribution appears excellent. However, as in the fast wind, there are also situations for which the core/beam distinction is more questionable. An example is given with AS2. Compared to VDF AS1 and AS3, the beam has been eroded and the phase space density within the gap between the core and the beam has been filled. In contrast, the non-Alfvénic slow wind, S, shows a more isotropic core distribution and the proton beam is not clearly separated.

The animation in the supplement material provides the respective dynamics of the core and beam linked to the passing of the strong Alfvénic fluctuations. In particular, it is interesting to note that the core of the distribution is apparently more dynamic than the beam, which is comparatively more stable in the RTN frame.

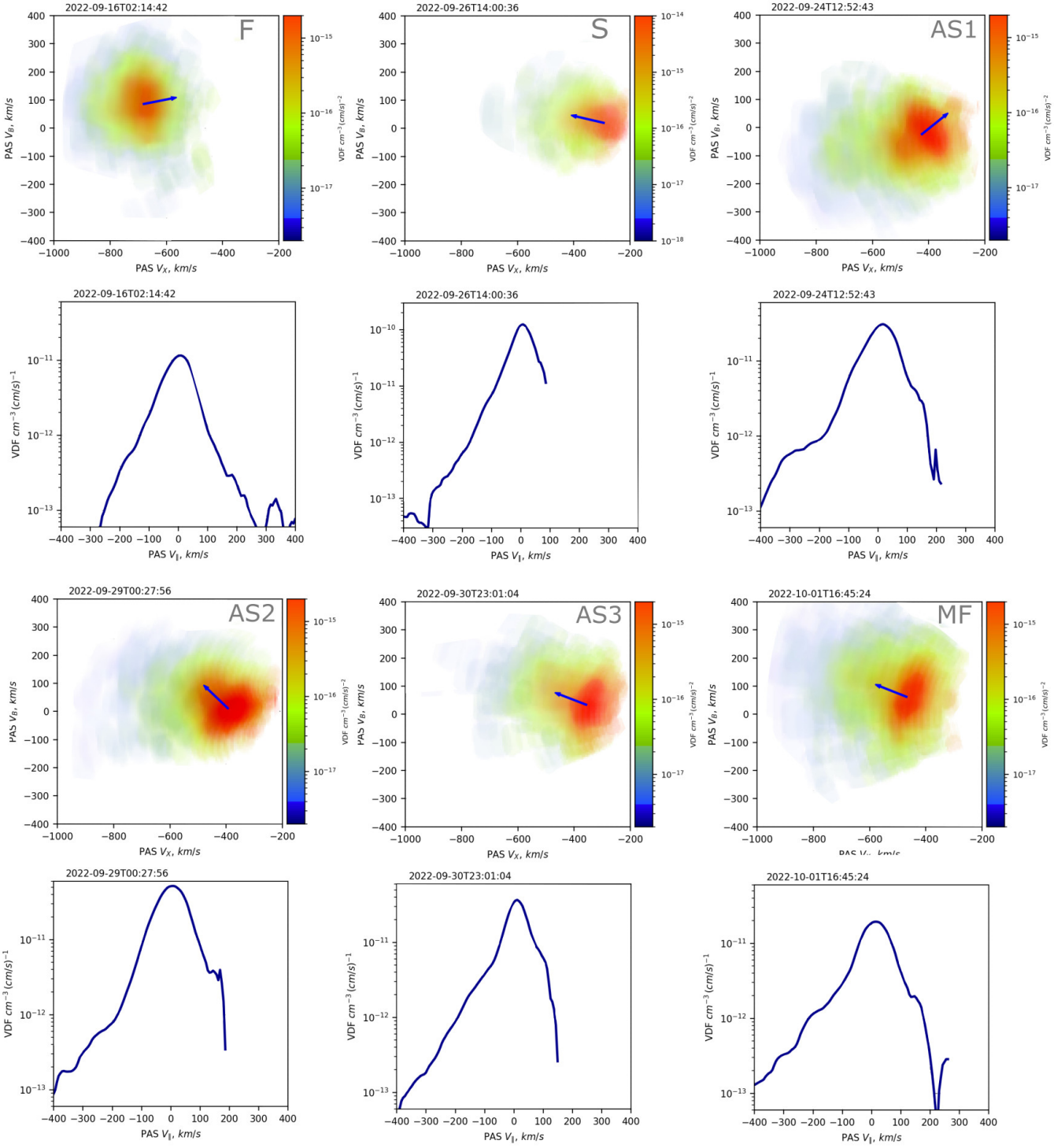


Fig. 5. SWA-PAS 2D and 1D velocity distribution functions (VDFs) for the selected intervals (see Figure 2). The 2D distributions are integrated onto the plane perpendicular to the $\mathbf{V} \times \mathbf{B}$ vector and include the solar wind bulk velocity vector. PAS 1D VDFs show the $V_\parallel$ cut of each VDF.

4. Investigation of Alfvénicity

Magnetic and velocity fluctuations can be fully characterized by performing a spectral analysis. A detailed investigation of the power spectra of the trace of magnetic field and solar wind velocity is deferred to a follow-up study, dedicated to the evolution of the power associated to solar wind fluctuations, to the slopes of the different frequency ranges and the breaks separating them as a function of the heliocentric distance. In this paper, instead, normalized power spectra of the trace of B and V are shown to compare the different streams avoiding the effect of the radial evolution (ΔR = 0.2 AU) that determines a different amplitude of the fluctuations in different streams. The normalized power spectra were computed in the following way. We derived the relative amplitude of the fluctuations from the Fourier analysis to compute the trace of magnetic field

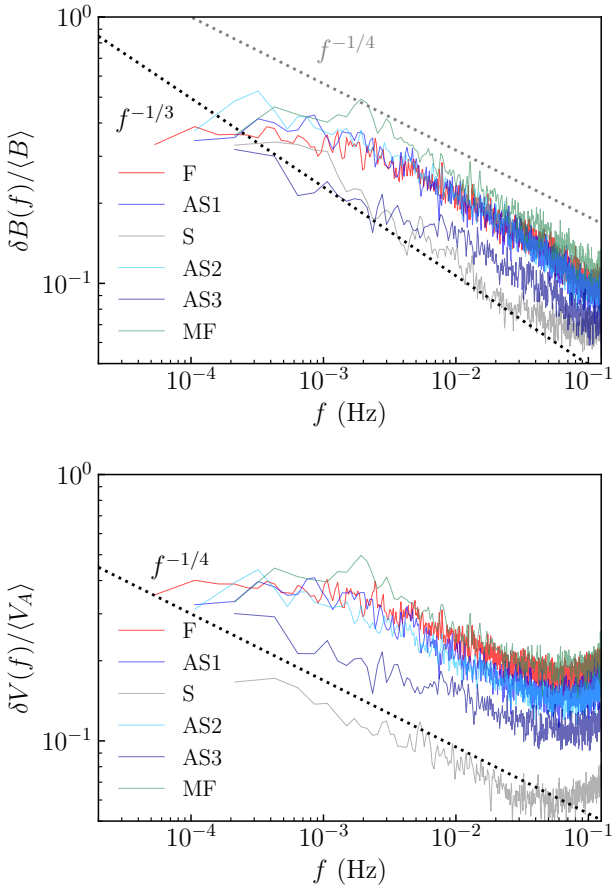


Fig. 6. Normalized power spectral density of the trace of magnetic field and solar wind velocity in the upper and lower panels respectively, for F (red), AS1 (dark blue), AS2 (light blue), AS3 (blue), MF (green), and S (gray) data intervals. The dashed lines indicate the typical slopes of the IK ($f^{-1/4}$) and K41 ($f^{-1/3}$) scalings.

as $\delta B(f)/\langle B\rangle = \sqrt{f S_B(f)}/\langle B\rangle$, where $S_B(f)$ is the trace of the power spectral density of the magnetic field components. In the same way, we derived $\delta V(f)/\langle V_A\rangle$. Normalizing to $\langle B\rangle$ and $\langle V_A\rangle$ allowed us to compare the fluctuations of different streams (Bruno et al. 2019; D'Amicis et al. 2020, 2022). The normalized power spectra ($\delta B(f)/\langle B\rangle$ and $\delta V(f)/\langle V_A\rangle$) in the upper and lower panels, respectively, are shown in Fig. 6. According to this normalization, Kolmogorov and Kraichnan scalings can be easily derived. Since $S_B(f) \sim f^{-5/3}$, $\delta B(f)/\langle B\rangle \sim f^{-1/3}$ for the Kolmogorov scaling. However, in the lower-frequency magnetohydrodynamic (MHD) range, $S_B(f) \sim f^{-3/2}$ or, equivalently, $\delta B(f)/\langle B\rangle \sim f^{-1/4}$, closer to the Kraichnan spectrum. The observation of two different sub-ranges within the inertial domain is in agreement with recent observations in the inner and outer heliosphere (Mondal et al. 2025; Wu et al. 2025), as well as previous Solar Orbiter observations (D'Amicis et al. 2025a). In a similar way, $\delta V(f)/\langle V_A\rangle \sim f^{-1/4}$ (since $S_V(f) \sim f^{-3/2}$) for the Kraichnan scaling. As expected, both the magnetic field and velocity normalized spectra show systematically lower values during the non-Alfvénic slow wind interval compared to the Alfvénic intervals, consistent with the reduced fluctuation amplitude and weaker Alfvénic content of the stream (e.g., Bruno & Carbone 2013). Moreover, the velocity power spectral densities tend to flatten at higher frequencies due to the onset of instrumental noise, consistent with previous studies (e.g., D'Amicis et al. 2022).

The v-b correlation coefficient reported in Fig. 2, used as a proxy to identify and select Alfvénic solar wind intervals, was computed at a fixed typical Alfvénic scale of 30 minutes. Similar to Marsch & Tu (1990a), in this section, we perform a spectral analysis using standard tools to study turbulence in the frequency domain: the normalized cross-helicity, σ_C, and the normalized residual energy, σ_R. As described in Appendix A, σ_C is derived from the Elsässer variables (Elsässer 1950) to investigate the Alfvénic content of solar wind fluctuations and the full range of frequencies where Alfvénicity is high (Tu et al. 1989; Grappin et al. 1991).

Since Alfvénic turbulence is characterized by high $v - b$ correlations along with weak compressibility, meaning that fluctuations in the magnitude of the magnetic field are much smaller than the fluctuations in the components of the magnetic field, magnetic compressibility is shown as well. This basically shows a fundamental property of Alfvénic fluctuations that they tend to stay in a state of spherical polarization (Bruno et al. 2001; Matteini et al. 2015). Magnetic compressibility, C_B, is defined as the ratio between the power spectral density of the magnitude of magnetic field over the trace of power spectral density of the magnetic field components.

Figure 7 shows σ_C (upper panels), σ_R (middle panels) and C_B (bottom panels) in the frequency domain of the different streams (same color code used throughout the paper). The comparison between the different streams shows a similar extension of the Alfvénic range that extends up to 4 $\times 10^{-2}$ Hz, in agreement with D'Amicis et al. (2025a). In general, all intervals show similar and high σ_C values in the range 2×10^{-4}–10^{-2} Hz, confirming previous observations by Helios (e.g., Tu & Marsch 1995) and recent findings by PSP (e.g., Thepthong et al. 2024; D'Amicis et al. 2025b). The decrease of σ_C toward zero at high frequencies is mainly linked to a flattening of the e^- spectrum rather than to a reduction of the e^+ component (D'Amicis et al. 2022, 2025a). This behavior has been interpreted either as the result of parametric decay of outward-propagating Alfvénic fluctuations (Tu et al. 1989; Galeev & Oraevskii 1963) or as the effect of compressive structures contributing (Marsch & Tu 1990b), related to magnetoacoustic waves, pressure-balanced structures (Goldstein & Siscoe 1972), or fine-scale stream tubes (Thieme et al. 1987). Alternatively, it may reflect enhanced compressive magnetic fluctuations rather than locally generated inward Alfvénic modes (Bruno et al. 1989), with the e^- spectrum possibly arising from magnetic field directional turnings (MFDT) in a turbulence regime dominated by outward Alfvén waves and convected structures (Tu & Marsch 1991). Although a correlation between inward Alfvénic fluctuations and density fluctuations has been reported (Grappin et al. 1990), caution is required as instrumental effects may produce artificial spectral and kinetic signatures that can mimic physical processes (De Marco et al. 2020).

On the other hand, σ_R is close to zero in the frequency range 10^{-3}–10^{-2} Hz for AS1, AS3, and MF, with slightly negative values at lower frequencies. In contrast, AS2 shows $\sigma_R < 0$ across the entire frequency range, indicating a dominance of magnetic over kinetic energy, while the fast wind exhibits predominantly positive values, suggesting a kinetic energy excess. This apparent kinetic imbalance in the fast wind is likely related to the omission of alpha particles in the present analysis, as discussed in Appendix B. Overall, the fast wind and most Alfvénic slow wind intervals analyzed here appear closer to each other in terms of residual energy than previously reported. This differs from previous studies, which found fast wind intervals closer to energy equipartition both at L1 (D'Amicis et al. 2022) and at ~0.35 AU

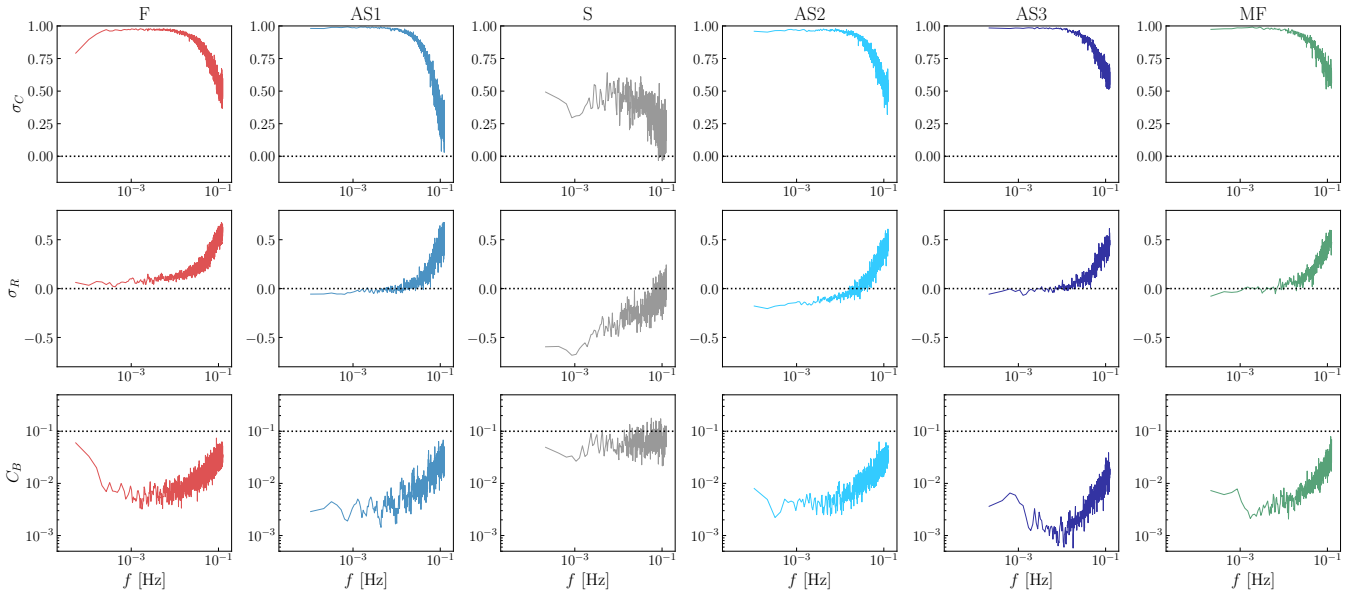


Fig. 7. Normalized cross-helicity, σ_C (upper), normalized residual energy, σ_R (middle), and magnetic compressibility C_B (lower) in the frequency domain for the fast wind (red), for the different Alfvénic slow wind streams, AS1-AS3 (different shades of blue), non-Alfvénic slow wind, S (gray), and for the MF (green) solar wind interval.

(D'Amicis et al. 2025a), while the Alfvénic slow wind exhibits a more pronounced magnetic energy excess even near perihelion. Such differences have been interpreted as evidence of a relatively rapid departure from equipartition, possibly driven by local compressive effects (D'Amicis et al. 2025a).

In contrast, the non-Alfvénic slow wind, S, is characterized by very low σ_C and persistently negative σ_R, reflecting a strong reduction of Alfvénic correlations and a dominance of magnetic fluctuations over kinetic energy. This behavior is consistent with a more compressive and evolved plasma, in which convected structures and compressive modes become increasingly important (Bruno & Carbone 2013).

5. Electron VDFs measured by SWA-EAS

Figure 8a shows the time series of the plasma proton speed for the period from 14 September to 2 October. The shaded regions again mark the selected intervals of interest (similar to the top panel in Figure 2). The blue traces in panels b and c show time series of the plasma core electron density N_e and temperature T_e, respectively, along with the corresponding protons parameters (black traces). These electron core parameters were determined by fitting an 1D, nondrifting Maxwellian distribution function model to the thermal energy range of the observed electron phase space density. The energy range <12 eV was excluded from this fitting analysis, since below this energy we observe mostly secondary- and photo-electrons emitted by the spacecraft (Nicolaou et al. 2021; Štverák et al. 2025). Moreover, the phase space density we used for the fitting analysis was corrected for the spacecraft potential (Lavraud & Larson 2016). We also scaled the determined N_e with a factor (constant for the entire interval) that accounts for uncertainties in the absolute gain of the sensors, and brings the plotted values to be consistent with the N_p levels. Although this is based on the assumption that $N_e \sim N_p$, for our purposes, however, it is more important that we find a very similar variation of N_e and N_p, which validates the accuracy of the determined parameters. Interestingly, the temperature of the two species does not show a correlation in their variation. The plasma electrons behave much more isothermally across the entire interval. For the fast solar wind intervals, T_e is often smaller that T_p. In the slow wind intervals ($V_{SW} < 400\,\mathrm{km\,s^{-1}}$), however, T_p exceeds T_e.

We further constructed the 2D pitch-angle versus energy distribution function of the solar wind electrons, taking into account the average magnetic field direction during the acquisition of each SWA-EAS measurement sample. Figure 8d shows the time series of the pitch angle distribution of electrons with energies $\gtrsim 69$ eV. At this energy range we clearly observe the field-aligned electron beams (strahl). Although there is variability of the strahl pitch angle distribution, we observe that for the selected intervals, there is a rather distinct and persistent phase space density peak along the parallel (0°), or antiparallel (180°) directions. We also observe a change of the beam direction, from parallel to antiparallel, at the beginning of 26 September, 2022. This change occurs across the reversal of the radial magnetic field component, exactly as expected for electron beams flowing along open field lines, since the beam is flowing radially outward (Owens & Forsyth 2013). The observed enhancement of proton density along with the B_R and beam direction reversals, is consistent with a current sheet crossing. In Figures 8e and f, we show examples of the full pitch-angle versus energy (speed) distribution averaged over two sub-intervals (one in the fast stream marked F and the other in AS2) that are indicated by the two vertical magenta ribbons. Both examples show a clear beam signature. In the first case the beam is peaked along the magnetic field direction, while in the second case it is flowing in the antiparallel direction.

We provide an animation in the supplementary material that shows the evolution of the 2D pitch-angle versus energy distribution throughout the entire interval. An examination of the electron PADs across the entire interval, as presented in this animation, shows that in numerous cases within the (non-Alfvénic) slow solar wind (i.e., many periods outside the selected intervals marked in Figures 2 and 8), the electron beams do not stand-out as a prominent feature as much as they do during the highlighted

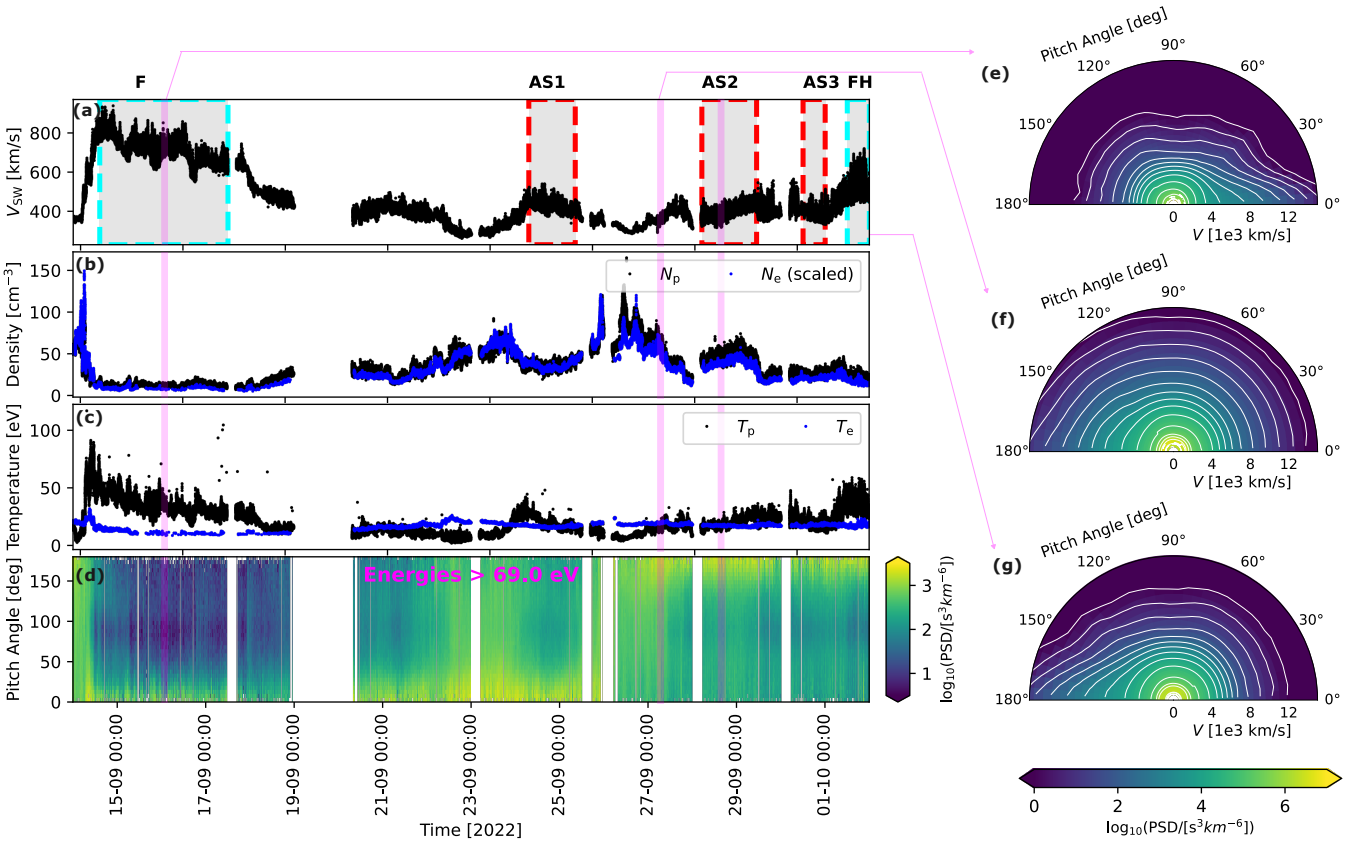


Fig. 8. Time series of (a) proton speed, (b) electron (blue) and proton (black) densities, (c) electron (blue) and proton (black) temperatures, (d) pitch-angle distribution of strahl electrons for energies >69 eV, (e) a 2D gyrotropic, pitch-angle vs. energy distribution averaged over a sub-interval in the middle of the fast wind interval, (f) a distribution for the non-Alfvénic slow wind (S) interval, and (g) a distribution for a sub-interval within the AS2 interval. PSD indicates phase space density.

sub-intervals. We seek to quantify these statements by fitting the strahl population observed throughout this entire interval using the method described in Owen et al. (2022) and examining the differences in strahl width and relative intensity with respect to the concurrent halo population. These parameters were derived from fits to the pitch angle distribution for E $\gtrsim$ 70 eV, with the latter derived from the relative intensity of the near field-aligned (or anti-aligned) flux compared to that observed for particles moving near-perpendicular to the field. For visibility purposes, we averaged the electron PADs over five-minute intervals within each separate region and present a scatter plot of our results in the main panel of Figure 9. In this plot, we recorded the averaged fits within each of the regions identified above by a colored point: Black points – S (211 5 minute averages of fitted samples); Blue points - F (827 averages); Red points - AS1 (302 averages); Green points - AS2 (356 averages); Magenta points - AS3 (143 averages); Cyan points - MF (142 averages)). There are also 2352 averaged samples which fall outside of the identified regions during the period of interest, but these are not included in the scatter-plot for reasons of clarity. They are however included alongside the S samples in the black traces in the sub-plots above and to the right of the main panel, which show the percentage of a given sample set falling within column-summed and row-summed data bins respectively. Otherwise, the same color scheme as used in the main panel is deployed in these subplots: The upper panel shows percentages of measured points falling in each of 50 logarithmically spaced bins in the range 10–100°), while the right panel shows the percentage of samples falling within one of 60 logarithmically spaced relative intensity bins in range 0.1–100. From Figure 9, it is clear that the F and MF intervals typically exhibit narrower and more intense beams than the other identified (AS) regions, or indeed the background slower solar wind. The most typical beam width for the three AS regions is similar, and similar also to the slow wind observations, although their typical intensity may be slightly lower than in the slow wind where a strahl population is identified (relative intensity values near 1 in this analysis suggest that the distribution is near isotropic in this energy range, such that no field aligned beam stands out from the halo population).

The comparison here between the fast and non-Alfvénic slow wind is consistent with the results of Pilipp et al. (1987a) and Owen et al. (2022) who report more highly collimated, narrow strahl in fast solar wind streams, but broader, or even fully isotropized distributions at strahl energies in slower winds. Although collimated beams appear in both fast and Alfvénic slow wind streams in our interval of interest, the latter are typically broader and less intense than in the former stream. This may indicate that the Alfvénic slow wind streams may have experienced more intense and/or longer duration scattering processes on their journey to the measurement point. The electron populations within the highlighted sub-intervals thus may typically carry more heat flux when compared to those within the non-Alfvénic streams within the examined interval.

On the other hand, there is no significant difference between the core electron temperature T_e during the highlighted intervals and T_e during the slow, non-Alfvénic wind time periods. In addition, the T_e variations are significantly smaller than the observed T_p variations within the entire interval. However, since T_e was

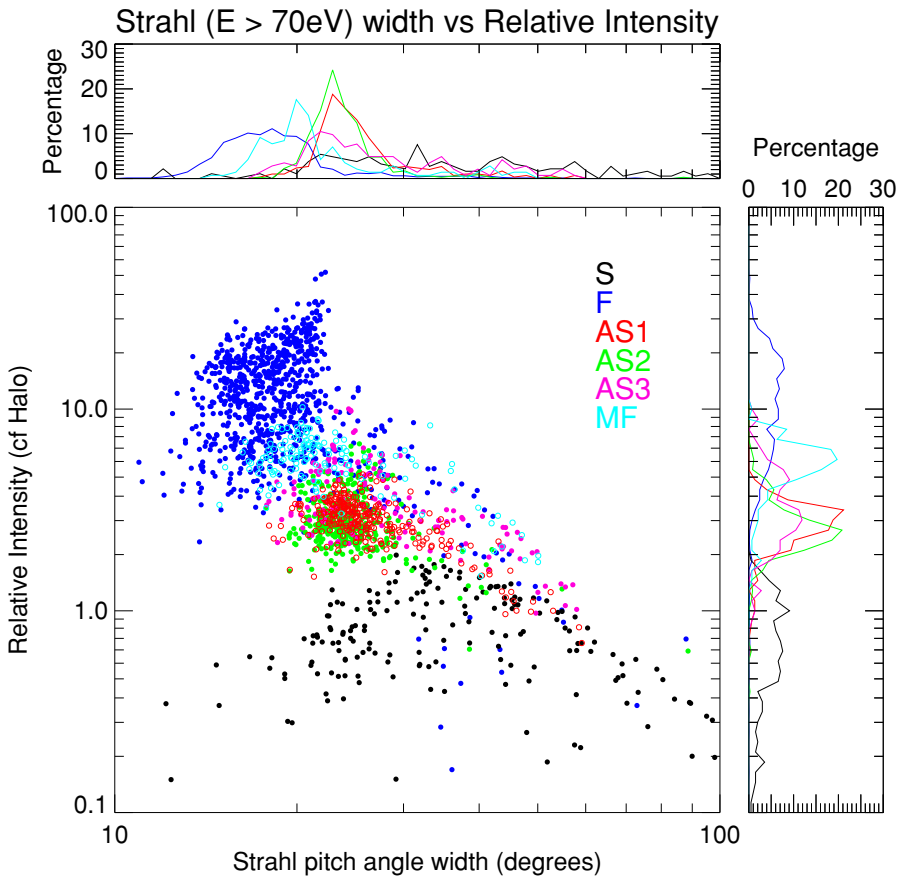


Fig. 9. Main panel: scatter plot of results of fitting analysis to the SWA-EAS strahl electron (E $\gtrsim$ 69 eV) pitch angle distribution. The horizontal axis indicates the fitted pitch angle width of an individual sample, with the vertical axis representing the relative intensity of the sampled strahl beam with respect to the concurrent halo population. Upper panel: histograms of the percentage of samples falling within one of 50 logarithmically spaced pitch angle bins in range (10–100°). Right panel: histograms of the percentage of samples falling within one of 60 logarithmically spaced relative intensity bins in range 0.1–100. In each of the three panels, the different regions identified within the overall period of interest are represented by different colors: Black S; Blue F; Red AS1; Green AS2; Magenta AS3; Cyan MF. All points that fall outside the specified periods of interest are included along with the S samples under the black traces in the histogrammed plots, although these are suppressed from the main scatterplot panel for clarity.

calculated using the preliminary calibration factors and assuming a nondrifting isotropic Maxwellian core, further studies are needed to properly quantify the electron bulk parameters.

6. Solar wind composition measured by SWA-HIS

We used the composition information in Figure 2 to support the identification of the intervals under study. Values in both the O^{7+}/O^{6+} and C^{6+}/C^{5+} charge state ratio panels are lower in the interval marked as F than during most of the remaining analyzed period, consistent with the typical composition of fast wind originating from coronal holes (von Steiger & Zurbuchen 2011). In contrast, during the AS1, AS2, AS3 intervals, the O and C ratios are clearly higher, reflecting values that are more similar to what would be expected for the slow, or non-coronal hole related solar wind (Geiss et al. 1995a). While the actual O ratio during AS1, AS2, AS3 may not be above the 0.145 slow solar wind threshold reported in Zhao et al. (2009), the non-Alfvénic slow wind interval, S, does exceed this threshold, consistent with its expected slow wind composition. Nevertheless, the AS intervals still exhibit a composition more closely associated with slow solar wind conditions. Lepri et al. (2013) showed that composition ratios evolve over the solar cycle in both the slow and fast wind, and that, along with any differences in instrumentation characteristics between ACE/SWICS and SWA-HIS, may contribute to uncertainties in the absolute values of the ratios. The MF interval has C and O ratios that lie between slow wind values and fast wind values. Since O and C ratios are believed to freeze-in at similar heights in the low corona (Buergi & Geiss 1986; Chen et al. 2003; Landi et al. 2012), these ratios have been observed to be generally well correlated in long-base line studies, with the exception of the outlier wind (Zhao et al. 2017). In the case of the outlier solar wind, the C ratio is observed to break the correlation with the O ratio and has much lower values than expected. Occurring primarily in slow solar wind and at the higher O ratio values, these low C ratio values are thought to be associated with a depletion in the density of fully stripped C^{6+} (see Zhao et al. 2017).

An examination of the C and O ratio correlation for the five Alfvénic intervals is shown in Figure 10. The F interval (blue) is clearly separated from the other intervals AS1-3 and MF, which partially overlap one another in this space. Furthermore, it can be seen from the correlation of these clusters of C and O ratios that these intervals do not fall into the ranges typical of outlier wind which extend to lower values of C^{6+}/C^{5+}, while maintaining higher values of O^{7+}/O^{6+}. The MF interval appears quite close in composition to the AS intervals, though its speed is closer to that of the fast interval, which is why it received a

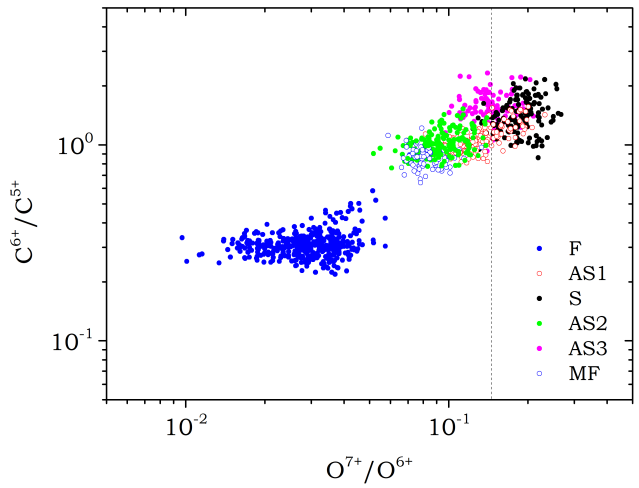


Fig. 10. Scatter plot of oxygen ratio (O^{7+}/O^{6+}) vs. carbon ratio (C^{6+}/C^{5+}) for the selected intervals: F (blue), AS1 (red), AS2 (green), AS3 (magenta), MF (empty blue), and S (black). The slow solar wind threshold reported in Zhao et al. (2009) is indicated as a dashed vertical line.

separate designation of MF. The separation between F and AS intervals is in contrast to a previous study using ACE data from 2002 (D'Amicis et al. 2019) where the fast and slow Alfvénic intervals were clustered together. The slow wind in that study had an O ratio closer to 1.0 and a C ratio near 5, and the fast and Alfvénic wind were clustered near an O ratio of 0.1 and a C ratio near 0.7. That study examined intervals during maximum of solar activity (2002) of solar cycle 23. In the current study, which is based on observations obtained during the ascending phase of solar cycle 25, the slow Alfvénic wind and the MF wind look much like the fast and Alfvénic wind from 2002. However, the F wind is very different, appearing at much lower O and C ratios than the 2002 wind. Based on the findings of Lepri et al. (2013), the O and C ratio in the fast solar wind are about a factor of 3–5 lower during solar minimum than during solar maximum. This appears to indicate that the much lower fast wind O and C ratios observed during our 2022 interval is more similar to solar minimum fast wind (coronal hole wind), while the 2002 fast wind is more similar to solar maximum fast wind. Based on the D'Amicis et al. (2019) paper and this current analysis, the Alfvénic slow wind occupies a composition regime in between the fast and slow solar wind. These results agree with recent work by Ervin et al. (2024), who showed composition characteristics of highly Alfvénic slow wind that was traced to an origin near an overexpanded coronal hole boundary. They also agree with Alterman (2025), who show that slow-intermediate speed solar wind is likely from coronal holes, but is not as "Alfvén wave rich" as that traditionally identified as fast wind due to differences in the source region topology.

7. Connecting to the solar sources

In the previous sections, we examined the in situ characteristics of different solar wind streams observed in situ by Solar Orbiter. Connecting a solar wind stream to its source of the Sun involves considerable uncertainties, associated both with the limited coverage of remote sensing observations from the solar surface to where measurements are made in situ as well as the lack of detailed, high-resolution, first principles plasma physics models of the solar wind expansion from the Sun into the supersonic solar wind. In this section, we provide a preliminary analysis of the possible origins at the Sun, i.e., the low coronal sources of such streams, deferring a detailed investigation to a companion paper (Panasenco et al., in prep.). A specific difficulty for the time intervals considered here is the fact that the in situ observations correspond to times when the coronal source regions were behind the solar disk as seen from Earth. This means that any magnetic field connection must rely on observations made either before, when that part of the Sun was visible from Earth, or later, after rotation has brought the source regions of the field back into view.

The first step in trying to determine the solar sources is to project the spacecraft position backward ballistically, using the solar wind speed measured at Solar Orbiter and solar rotation. To correct for solar wind acceleration and test the stability of the projection, the ballistic projection is also carried out adding speeds of up to ± 80 km s^{-1} in bins of 10 km s^{-1} (see, e.g., Panasenco et al. 2020, and references therein). The projection is stopped at a distance from the Sun, where a surface called the Source Surface is positioned, and which is determined empirically to best fit the magnetic structure with the observed solar corona. The magnetic field from the photosphere to the source surface, located for the present calculations at R = 2.5 $R_\odot$ from the Sun's center, is calculated using a potential field source surface (PFSS) extrapolation, with the model developed by (Schrijver & De Rosa 2003). As the name states, the magnetic field is assumed to be potential, and assimilates surface magnetic field data from the Solar Dynamic Observatory (SDO) Helioseismic and Magnetic Imager (HMI) with a six-hour cadence. To better capture both the polar field and the field evolution, the photospheric maps include the effects of both empirically determined differential rotation, meridional flow, and convective dispersal profiles, as well as a prescription for fragmentation and collision of flux.

Here we provide the mapping results using PFSS extrapolation for 2 October 2022, at the end of the in situ interval under investigation. The date was chosen as it provides the best instantaneous fit with the observed magnetic field polarities and structure observed at Solar Orbiter. A more detailed discussion with maps built on maps using magnetic field measurements at different times, both before and after the in situ measurements, including the difficulties and potential errors, may be found in Panasenco et al., in prep. Figure 11 shows B^2 contour maps and solar wind magnetic foot-points along Solar Orbiter trajectories (red) for the selected intervals. The direct projected position of Solar Orbiter onto the Sun is indicated by O and squares, while the crosses indicate the position of the ballistic projection onto the source surface (with correction speeds, so that there are 17 crosses for each O), while the lines from the crosses to the circles then indicate the mapping back from the source surface into the Solar corona, where contours of magnetic field intensity at a height of 1.2 R_s are plotted and the green and blue shading colors indicate opposite polarities. The dark bold lines indicate polarity inversion lines.

At the beginning of the studied interval, up until 17 September, Solar Orbiter was connected to a large coronal hole with wide southward extension through a corridor at 70° Carrington longitude. As Solar Orbiter's trajectory moved it through the corridor neck the wind speed slowed down and the density increased while remaining in the same polarity region until 26 September, when the HCS was crossed. The first Alfvénic slow interval AS1 had Solar Orbiter connected to relatively strong and rapidly expanding field in the corridor, while the slow wind interval marked as S on Figure 2 has Solar Orbiter having just crossed

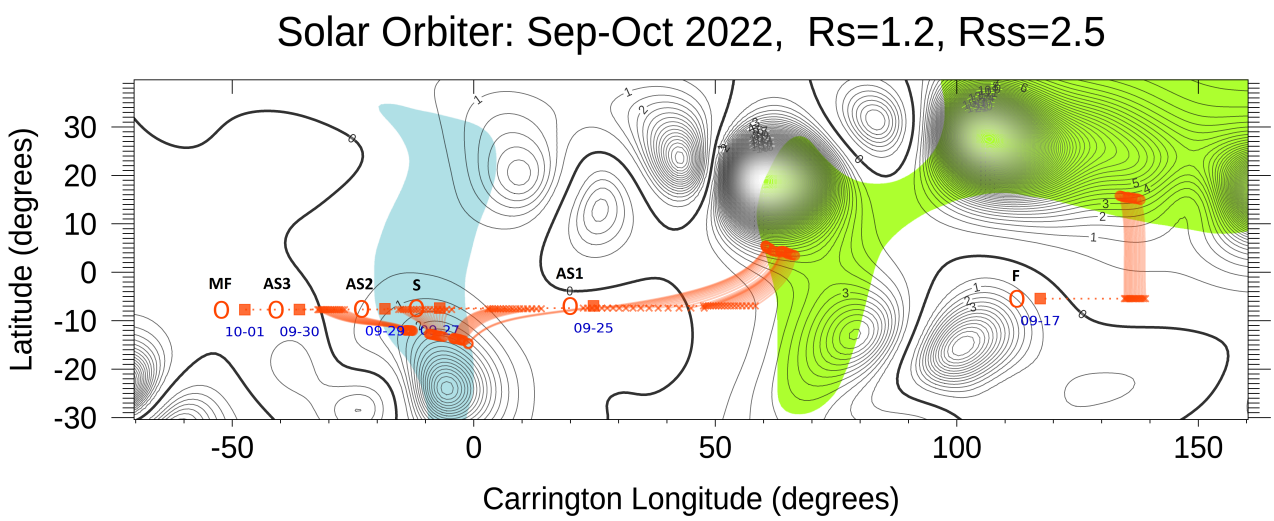


Fig. 11. Potential field source surface B^2 contour maps and solar wind magnetic foot-points along Solar Orbiter trajectories (red) for the selected intervals. The map shows magnetic pressure iso-contours calculated for the heights R = 1.2 $R_\odot$ and the projection of the s/c location (squares) on the source surface (crosses) and down to the solar wind source region (circles). The crosses result from ballistic mapping using the measured in situ solar wind speed and solar rotation ±80 km s^{-1} in bins of 10 km s^{-1}. Open magnetic field regions are shown in green (positive polarity) and cyan (negative polarity), while the neutral line is in black bold. The dates near the squares indicate the time of the corresponding in situ observations.

the HCS and having low Alfvénicity and higher densities, as expected. This is followed by AS2 on 29 September and AS3 ending on 1 October as Solar Orbiter approaches perihelion.

The transition from AS2 to AS3 is accompanied by a decrease in density as the source region connected to Solar Orbiter moves toward the center of the coronal hole and then the solar wind subsequently accelerates into MF. The relatively slow speed of AS2 and AS3 and their different densities may reflect the complexity of the magnetic field within the coronal hole, involving local embedded polarity inversions not extending into the heliosphere (i.e., pseudostreamers) as further explored in Panasenco et al., in prep. The above results are broadly in agreement with previous studies focused on the solar sources of Alfvénic streams (Bale et al. 2019; Panasenco et al. 2020; D'Amicis et al. 2021b; Ervin et al. 2024; D'Amicis et al. 2025a). While PSP observations broadly support the presence of a basal Alfvénic fluctuation flux at the source of the solar wind, they also support the idea that slow Alfvénic streams survive from rapidly expanding coronal holes or coronal hole corridors.

8. Discussion

The combined analysis of the observations from the three SWA sensors provides a coherent picture of the physical transition between fast wind, Alfvénic slow wind, and non-Alfvénic slow wind regimes. While almost all selected intervals exhibit signatures of Alfvénic fluctuations, the SWA observations indicate that the three solar wind regimes remain distinguishable in their kinetic, electron, and compositional properties.

The Alfvénic content of the fluctuations was investigated through the analysis of normalized cross-helicity and residual energy in the freqeuncy domain, in order to characterize the extent of the Alfvénic range within the different streams. Despite limitations imposed by instrumental noise at high frequencies, primarily affecting plasma measurements (see also D'Amicis et al. 2025a), the analysis reveals comparable extensions of the Alfvénic range across all intervals, allowing the investigation of fluctuations down to timescales on the order of minutes.

SWA-PAS measurements show that the proton VDFs are systematically anisotropic and characterized by the presence of proton beam populations drifting along the magnetic field at approximately 1.6–2V_A when the streams are Alfvénic (Feldman et al. 1973; Marsch et al. 1982b; Marsch and Livi 1987; Goldstein et al. 2000; Bruno et al. 2024; D'Amicis et al. 2025a). While the relative beam intensity and proton anisotropy vary across the different streams (Neugebauer & Snyder 1962, 1966; Asbridge et al. 1974; Yermolaev & Stupin 1997; Kasper et al. 2007; Bruno et al. 2024), the beam population appears more clearly developed in the most Alfvénic intervals. These features are consistent with previous observations linking proton beams and temperature anisotropies to large-amplitude Alfvénic fluctuations and wave–particle interactions occurring during solar wind expansion (Marsch et al. 1982b; Marsch and Livi 1987; Hellinger et al. 2006; Matteini et al. 2007; Bruno & Carbone 2013). In contrast, the non-Alfvénic slow wind exhibits weaker anisotropies and reduced beam contributions, consistent with a more collisionally processed plasma state.

SWA-EAS observations mainly focus on the behavior of strahl electrons, highlighted through 2-D pitch-angle distributions. Our results show that fast wind intervals are characterized by more intense and narrower pitch-angle widths strahl populations, while becoming weaker and progressively broader and in some cases nearly isotropic under standard slow wind conditions, indicative of stronger pitch-angle scattering and enhanced isotropization during solar wind expansion, consistent with earlier studies (Pilipp et al. 1987a; Owen et al. 2022). Moreover, the variation of the strahl width with radial distance has been investigated by a number of authors (e.g., Hammond et al. 1996; Anderson et al. 2012; Graham et al. 2017). Most recently, Owen et al. (2022) found that the average pitch angle width of these beams does not show significant evolution with distance, suggesting a balance between focusing and scattering processes across the covered distance range (~0.43 to ~1.0 AU). This general trend also aligns with kinetic-theory predictions (Horaites et al. 2018) and with radial evolution studies based on Helios measurements (Maksimovic et al. 2005), both of which show that strahl broadening is enhanced in higher-density, more collisional, and more turbulent solar wind.

Within this framework, the Alfvénic slow wind intervals identified in our analysis display electron properties intermediate between fast and standard slow wind. Although relatively collimated strahl populations are still observed, the corresponding beams are systematically broader and less intense than those measured in fast wind streams. This gradual transition suggests that electrons in Alfvénic slow wind may have undergone stronger or longer-duration pitch-angle scattering during their outward propagation. Such scattering may plausibly be associated not only with Coulomb collisions but also with wave–particle interactions, involving whistler-mode waves driven by heat flux instabilities (Roberg-Clark et al. 2018; López et al. 2019). These waves have been proposed as an efficient mechanism for regulating the heat flux and diffusing strahl electrons into the halo population. This observational evidence implies that the electron populations within the highlighted subintervals are capable of transporting a larger heat flux than those in the surrounding non-Alfvénic slow wind, reflecting significant differences in the efficiency of scattering and in the overall evolution of the suprathermal electron distribution within different solar wind regimes.

SWA/HIS independently reveals a similar compositional progression in the heavy ion properties. Fast wind intervals display low O and C charge-state ratios, consistent with typical coronal-hole-associated plasma observed during solar minimum conditions (Lepri et al. 2013), whereas non-Alfvénic slow wind exhibits enhanced charge-state ratios, exceeding the O^{7+}/O^{6+} slow wind threshold reported in Zhao et al. (2009) and associated with higher freeze-in temperatures. The Alfvénic slow wind intervals systematically occupy an intermediate compositional regime between these two limiting cases, supporting recent findings linking these intervals to solar wind originating near overexpanded coronal hole boundaries (Ervin et al. 2024). These compositional signatures are consistent with the idea that Alfvénic slow wind originates from plasma released along open magnetic field regions that differ from both the large coronal holes typically associated with fast wind and the hotter source regions commonly linked to non-Alfvénic slow wind.

Taken together, these observations suggest that Alfvénic slow wind retains several kinetic, electron, and compositional properties typically associated with more coronal hole-like wind despite its reduced bulk speed. This supports the interpretation of Alfvénic slow wind as plasma that preserves part of the coronal-hole source signature while undergoing a different acceleration and transport history during its expansion through the heliosphere, related to the magnetic field expansion profile as well as the complexity of the field itself, as measured by transverse gradients or other measures of mapping complexity, such as the squashing factor.

Such an interpretation is consistent with recent studies combining compositional and turbulence properties to identify solar wind source regions. Alterman & D'Amicis (2025a,b) showed that helium-rich and highly Alfvénic solar wind is generally associated with coronal-hole sources, whereas helium-poor and weakly Alfvénic plasma is more commonly associated with slow-wind source regions. Within this framework, plasma originating from typically slow-wind sources may reach speeds comparable to the lower-speed tail of coronal-hole-associated wind because of differences in the transit acceleration profiles experienced during heliospheric expansion (Halekas et al. 2023; Rivera et al. 2024a; Rivera, et al. 2025a). Altogether, these results support the interpretation that Alfvénic slow wind represents the low-speed extension of Alfvénic coronal-hole-associated plasma.

The coherent transition observed between suprathermal electron properties and heavy-ion composition is particularly significant. Charge-state ratios preserve the imprint of coronal plasma conditions at freeze-in, whereas proton and electron velocity distributions are continuously modified by Coulomb collisions, wave–particle interactions, magnetic focusing, and pitch-angle scattering during solar wind expansion. In principle, these transport processes could erase any direct relationship between the electron properties measured in situ and the original coronal source conditions. Instead, the combined SWA observations indicate that different solar wind streams retain different degrees of information about their solar origin. The persistence of the correspondence between suprathermal electron properties and heavy-ion composition suggests that at least part of the coronal-source information survives kinetic processing during heliospheric transport. In this framework, the transition observed in suprathermal electron properties has a clear counterpart in the compositional measurements, implying that some streams preserve source-related signatures more efficiently than others depending on both source-region topology and transport history, consistent with previous studies (Hefti et al. 1999; Macneil et al. 2020; Berčič et al. 2020; Wu et al. 2026).

The magnetic connectivity analysis is consistent with the different coronal source conditions inferred from the PFSS mapping. The fast wind interval maps back to a large low-latitude coronal hole, whereas the Alfvénic slow wind intervals are associated with open-field regions located in overexpanding coronal-hole corridors potentially associated with pseudostreamers. In particular, AS1 connects to a region characterized by a strong expansion factor, which may contribute to the reduced solar wind acceleration observed within the stream. Conversely, AS2, AS3, and MF connect to more extended open-field regions whose magnetic connectivity and expansion properties likely contribute to the transition toward faster wind (MF) conditions observed later in the interval.

Overall, the combined SWA observations suggest that Alfvénic fluctuations play an important role not only in shaping the local kinetic properties of the plasma, but also in regulating the extent to which coronal source signatures remain detectable during solar wind expansion. Understanding how turbulence, particle transport, and coronal magnetic connectivity jointly shape the evolution of solar wind plasma will be essential for clarifying the physical origin and evolution of Alfvénic slow wind.

9. Conclusion

In a broad statistical sense, the Alfvénic slow wind is emerging as a third class of solar wind characterized by bulk speeds typical of the slow wind, but with other properties typical of the fast wind. These differences likely reflect variations in the magnetic topology of the different solar wind source regions. Such variations would impact the processes that determine solar-wind charge-state and composition ratios (von Steiger et al. 2000; Geiss et al. 1995a,b; Xu & Borovsky 2015; Lepri et al. 2013; Zhao et al. 2022; Alterman et al. 2025a; Shi et al. 2025) and also the Alfvénic content of the solar wind, which in turn affects its transit acceleration profiles (Alterman 2025; Halekas et al. 2023; Rivera et al. 2024a; Rivera, et al. 2025a).

Within this framework, we have analyzed three Alfvénic slow wind streams together with a fast wind stream, one moderate fast stream, and a non-Alfvénic slow wind interval observed by Solar Orbiter between 0.59 and 0.38 AU from 14 September to 2 October. By combining measurements from all SWA

sensors with turbulence and magnetic connectivity analyses, we investigated proton and electron velocity distributions, heavy-ion charge-state composition, and the spectral properties of the observed streams in order to relate their kinetic and compositional signatures to their source regions.

The results reveal a coherent transition between the fast, Alfvénic slow, and non-Alfvénic slow wind regimes. In particular, the Alfvénic slow wind intervals preserve several proton, electron, compositional, and turbulence properties commonly associated with coronal-hole-associated plasma despite their reduced bulk speed, supporting the view that the Alfvénic slow wind represents the low-speed extension of fast coronal-hole-associated wind. At the same time, significant differences persist among streams observed at comparable heliocentric distances and associated with similar coronal source regions, suggesting that both source-region topology and interplanetary transport processes contribute to shaping the observed solar wind properties.

An important open question emerging from this work is the apparent lack of radial evolution commonly expected for Alfvénic solar wind turbulence. Most Alfvénic intervals remain close to energy equipartition despite their different heliocentric distances and solar wind bulk speeds. Remarkably, AS2 and AS3, although observed at comparable heliocentric distances and associated with similar coronal source regions, display significantly different energy balances, in agreement with recent near-Sun observations reporting substantial variability in magnetic field fluctuation amplitudes within streams originating from similar source regions (Rivera et al. 2024b). This finding contrasts with previous observations and theoretical expectations, which predict a progressive reduction of Alfvénicity and an increasing departure from energy equipartition with heliocentric distance (Marsch & Tu 1990a; Bruno et al. 2007; D'Amicis et al. 2022). Previous studies combining measurements at different heliocentric distances (e.g., D'Amicis et al. 2022, 2025a) also suggest a gradual shift of the Alfvénic range toward lower frequencies during solar wind expansion. In the present work, however, despite the ~0.2 AU radial excursion covered by Solar Orbiter, such trends are not clearly observed.

This suggests that the variability among the different streams cannot be explained solely in terms of radial evolution, but likely reflects additional processes related to solar wind acceleration, transport, and source-region properties (Halekas et al. 2023; Rivera et al. 2024a; Alterman 2025). Understanding why some Alfvénic streams remain close to energy equipartition whereas others evolve differently therefore remains a major open problem. Future investigations combining turbulence properties, helium abundance (Alterman 2025; Alterman & D'Amicis 2025a; Alterman et al. 2025a,b; Alterman & D'Amicis 2025b), composition measurements, and magnetic connectivity analyses will be essential to clarifying the interplay between coronal source conditions, interplanetary transport, and the evolution of Alfvénic solar wind streams.

These findings also present a wide range of challenges to existing models of the solar wind, particularly in explaining how Alfvénicity can be maintained within slow solar wind streams that originate from distinct regions on the Sun. The stationarity or evolution of the solar source could partly explain why Alfvénicity can be maintained or be lost within slow solar wind streams when observed at different heliocentric distances (e.g., D'Amicis et al. 2021a). However, one should also take into account local inhomogeneities that would determine the degradation of v-b correlations, for example the presence of compressible phenomena (e.g., Bruno & Bavassano 1991). In particular, it is unclear why, in some regions, the solar wind remains highly Alfvénic as it propagates away from the Sun. On the other hand, under which conditions and why some Alfvénic streams depart from energy equipartition and thus show a different behavior with respect to previous cases (e.g., Tu & Marsch 1995; D'Amicis et al. 2022, 2025a) is still not understood and needs further investigation. This raises fundamental questions about the interplay between magnetic field topology, wave-particle interactions, coronal heating processes, and the role of turbulence and compressions in shaping solar wind properties. The fact that Alfvénic fluctuations persist across the heliosphere suggests the presence of robust and possibly universal mechanisms operating in the early phases of solar wind formation and acceleration. High-resolution measurements from Solar Orbiter, combined with those from PSP, will provide unprecedented access to the inner heliosphere, allowing scientists to probe the nascent solar wind closer to its source than ever before with particular reference to the Alfvénic solar wind in a broad range of heliocentric distances and temporal scales. Despite these observational advances, more statistics are needed and the combined observations from all the SWA sensors are crucial in order to study the underlying physical processes that give rise to the variety of outcomes observed in solar wind streams that are still not fully understood.

Data availability

The animated sequences are available at `https://www.aanda.org`

Acknowledgements. Solar Orbiter is a mission of international cooperation between ESA and NASA, operated by ESA. Solar Orbiter SWA data were derived from scientific sensors that were designed and created and are operated under funding provided by numerous contracts from UKSA, STFC, the Italian Space Agency, CNES, the French National Centre for Scientific Research, the Czech contribution to the ESA PRODEX program, and NASA. Solar Orbiter SWA work at INAF/IAPS is currently funded under ASI grant 2018-30-HH.1-2022. Solar Orbiter SWA work at the UCL/Mullard Space Science Laboratory is currently funded by STFC (grant Nos. ST/W001004/1 and ST/X/002152/1). This research was supported by the International Space Science Institute (ISSI) in Bern through the ISSI International Team projects #550 "Solar Sources and Evolution of the Alfvénic Slow Wind", #560 "Turbulence at the Edge of the Solar Corona: Constraining Available Theories Using the Latest Parker Solar Probe Measurements", and #23-591 "Evolution of Turbulence in the Expanding Solar Wind". L.S.V. was supported by the Swedish Research Council (VR) Research Grant N. 2022-03352, and by the projects "2022KL38BK– The ULtimate fate of TuRbulence from space to laboratory plAsmas (ULTRA)" (B53D23004850006) and 'Data-based predictions of solar energetic particle arrival to the Earth: ensuring space data and technology integrity from hazardous solar activity events' (H53D23011020001), funded by the Italian Ministry of University and Research through PRIN/NRRP-NextGenerationEU.

References

Abbo, L., Ofman, L., Antiochos, S. K., et al. 2016, Space Sci. Rev., 201, 55
Alterman, B. L. 2025, ApJ, 984, L64
Alterman, B. L., & D'Amicis, R. 2025a, ApJ, 982, L40
Alterman, B. L., & D'Amicis, R. 2025b, ApJ, 996, L12
Alterman, B. L., & Kasper, J. C. 2019, ApJ, 879, 6
Alterman, B. L., Kasper, J. C., Stevens, M. L., & Koval, A. 2018, ApJ, 864, 112
Alterman, B. L., Kasper, J. C., Leamon, R. J., & McIntosh, S. W. 2021, Sol. Phys., 296, 67
Alterman, B. L., Rivera, Y. J., Lepri, S. T., & Raines, J. M. 2025a, A&A, 694, 265
Alterman, B. L., Rivera, Y. J., Lepri, S. T., Raines, J. M., & D'Amicis, R. 2025b, A&A, 700, A23
Anderson, B. R., Skoug, R. M., Steinberg, J. T., & McComas, D. J. 2012, J. Geophys. Res., 117, A4
Anselmet, F., Gagne, Y., Hopfinger, E. J., & Antonia, R. A. 1984, J. Fluid Mech., 140, 63
Antiochos, S. K., Mikic, Z., Titov, V. S., Lionello, R., & Linker J. A. 2011, ApJ, 731, 112

Antonucci, E., Abbo, L., & Dodero, M. A. 2005, A&A, 435, 699
Asbridge, J. R., Bame, S. J., & Feldman, W. C. 1974, Sol. Phys., 37, 451
Bale, S. D., Badman, S. T., Bonnell, et al. 2019, Nature, 576, 237
Bale, S. D., Horbury, T. S., Velli, M., et al. 2021, ApJ, 923, 174
Bale, S. D., Drake, J. F., McManus, M. D., et al. 2023, Nature, 618, 252
Barndorff-Nielsen, O. E. 1997, Scandinavian J. Stat., 24, 1
Barndorff-Nielsen, O. E., Jan Pedersen, J, & Sato, K.-I. 1997, Adv. Appl. Probab., 33, 160
Bavassano, B., & Bruno, R. 1991, J. Geophys. Res.96, 1737
Bavassano, B., & Bruno, R. 2000, J. Geophys. Res., 105, 5113
Bavassano, B., Woo, R., & Bruno, R. 1997, Geophys. Res. Lett., 24, 1655
Bavassano, B., Pietropaolo, E., & Bruno, R. 1998, J. Geophys. Res., 103, 6521
Bavassano, B., Pietropaolo, E., & Bruno, R. 2000, J. Geophys. Res., 105, 12697
Belcher, J. W., & Davis, L. 1971, J. Geophys. Res., 76, 3534
Belcher, J. W., & Solodyna, C. V. 1975, J. Geophys. Res., 80, 181
Belcher, J. W., Davis, L. Jr., & Smith, E. J. 1969, J. Geophys. Res., 74, 2302
Berčič, L., Larson, D., Whittlesey, P., et al. 2020, ApJ, 892, 88
Borovsky, J. E. 2012, J. Geophys. Res., 117, A05104
Borovsky, J. E. 2016, J. Geophys. Res., 121, 5055
Brodiano, M., Dmitruk, P., & Andrés, N. 2023, Phys. Plasmas, 30, 032903
Brown, C. P., Maruca, B. A., Prabakaran, V., et al. 2025, Geophys. Res. Lett., 52, e2025GL115186
Bruno, R. 2019, Earth Space Sci., 6, 656
Bruno, R., & Bavassano, B. 1991, J. Geophys. Res., 96, 7841
Bruno, R., & Carbone, V. 2013, Liv. Rev. Sol. Phys., 10, 2
Bruno, R., & Trenchi, L. 2014, ApJ, 787, L24
Bruno, R., Bavassano, B., & Villante, U. 1985, J. Geophys. Res., 90, 4373
Bruno, R., Villante, U., Bavassano, B., Schwenn, R., & Mariani, F. 1986, Sol. Phys., 104, 431
Bruno, R., Bavassano, B., Rosenbauer, H., & Mariani, F. 1989, Adv. Space Res., 9, 131
Bruno, R., Carbone, V., Veltri, P., Pietropaolo, E., & Bavassano, B. 2001, Plan. Space Sci., 49, 1201
Bruno, R., Carbone, V., Sorriso-Valvo, L., & Bavassano, B. 2003, J. Geophys. Res., 108, 1130
Bruno, R., D'Amicis, R., Bavassano, B., Carbone, V., & Sorriso-Valvo, L. 2007, Anna. Geophys., 25, 1913
Bruno, R., Telloni, D., Sorriso-Valvo, L., et al. 2019, A&A, 627, A96
Bruno, R., De Marco, R., D'Amicis, R., et. al. 2024, ApJ, 969, 106
Buergi, A., & Geiss, J. 1986, Sol. Phys., 103, 347
Camporeale, E., Caré, A., & Borovsky, J. E. 2017, J. Geophys. Res., 122, 10910
Callahan, Steven P., Callahan, Jason H., Scheldegger, Carlos E., et al. 2008, Comput. Sci. Eng., 10, 88
Carbone, F., & Sorriso-Valvo, L. 2014, Eur. Phys. J. E, 37, 61
Chen, Y., Esser, R., & Hu, Y. 2003, ApJ, 582, 467
Chen, C. H. K., Bale, S. D., Bonnell, J. W., et al. 2020, ApJS, 246, 53
Coleman, P. J. 1968, ApJ, 153, 371
D'Amicis, R., & Bruno, R. 2015, ApJ, 805, 84
D'Amicis, R., Bruno, R., & Bavassano, B. 2007, Geophys. Res. Lett., 34, 5108
D'Amicis, R., Bruno, R., & Bavassano, B. 2011, J. Atmos. Sol.-Terr. Phys., 2011, 3, 653
D'Amicis, R., Matteini, L., & Bruno, R. 2019, MNRAS, 483, 4665
D'Amicis, R., Matteini, L., Bruno, R., & Velli, M. 2020, Sol. Phys., 295, 46
D'Amicis, R., Perrone, D., Velli, M., & Bruno, R. 2021a, J. Geophys. Res., 126, e2020JA028996
D'Amicis, R., Bruno, R., Panasenco, O., et al. 2021b, A&A, 656, A21
D'Amicis, R., Perrone, D., Velli, M., et al. 2022, Universe, 8, 352
D'Amicis, R., Velli, M., Panasenco, O., et al. 2025a, A&A, 693, A243
D'Amicis, R., Sorriso-Valvo, L., Benella, S., et al. 2025b, A&A, accepted
De Marco, R., Bruno, R., D'Amicis, R., Telloni, D., & Perrone, D. 2020, A&A, 639, A82
De Marco, R., Bruno, R., Krishna Jagarlamudi, V., et al. 2023, A&A, 669, A108
Dmitruk P., & Matthaeus W. H. 2007, Phys. Rev. E, 76, 036305
Dudok de Wit, T., Krasnoselskikh, V. V., Bale, S. D., et al. 2020, ApJS, 246, 39
Elliott, H. A., McComas, D. J., & Riley, P. 2003, Ann. Geophys., 21, 1331
Elsässer, W. M. 1950, Phys. Rev., 79, 183
Ervin, T., Bale, S. D., Badman, S. T., et al. 2024, ApJ, 969, 83
Feldman, W. C., Asbridge, J. R., Bame, S. J., & Montgomery, M. D. 1973, J. Geophys. Res., 78, 2017
Feldman, W. C., Asbridge, J. R., Bame, S. J., & Montgomery, M. D. 1974, Rev. Geophys. Space Phys., 12, 715
Feldman, W. C., Asbridge, J. R., Bame, S. J., Montgomery, M. D., & Gary, S. P. 1975, J. Geophys. Res., 80, 4181
Feldman, W. C., Asbridge, J. R., Bame, S. J., Gosling, J. T., & Lemons, D. S. 1978, J. Geophys. Res., 83, 5285
Feldman, U., Landi, E., & Schwadron, N.A. 2005, J. Geophys. Res., A110 7109
Feynman, J. 1975, Sol. Phys., 43, 249
Fitzenreiter, R. J., Ogilvie, K. W., Chornay, D. J., & Keller, J. 1998, Geophys. Res. Lett., 25, 249
Fox, N. J., Velli, M. C., Bale, S. D., et al. 2016, Space Sci. Rev., 204, 7
Frisch, U. 1995, Turbulence, Cambridge University Press, Cambridge, UK
Fu, H., Madjarska, M. S., Li, B., Xia, L., & Huang, Z. 2018, MNRAS, 478, 1884
Galeev, A. A., & Oraevskii, V. N. 1963, Sov. Phys. Dokl., 7, 988
Gary, S. P., Goldstein, B. E., & Steinberg, J. T. 2001, J. Geophys. Res., 106, 24955
Geiss, J., Gloeckler, G., & von Steiger, R. 1995a, Space Sci. Rev., 72, 49
Geiss, J., Gloeckler, G., von Steiger, R., et al., 1995b, Science, 268, 1033
Gloeckler, G., Cain, J., Ipavich, F. M., et al. 1998, Space Sci. Rev., 86, 497
Goldstein, B., & Siscoe, G. L. 1972, NASA SP, 308, 506
Goldstein, B. E., Neugebauer, M., & Smith, E. J. 1995, Geophys. Res. Lett., 22, 3389
Goldstein, B., Neugebauer, M, Zhang, L. D., & Gary, S. P. 2000, Geophys. Res. Lett., 27, 53
Gosling, J. T., Baker, D. N., Bame, S. J., et al. 1987, J. Geophys. Res., 92, 8519
Graham, G. A., Rae, I. J., Owen, C. J., et al., 2017, J. Geophys. Res., 122, 3858
Grappin, R., Mangeney, A., & Marsch, E. 1990, J. Geophys. Res., 95, 8197
Grappin, R., Velli, M., & Mangeney, A. 1991, Ann. Geophys., 9, 416
Halekas, J. S., Bale, S. D., Berthomier, M., et al. 2023, ApJ, 952, 26
Hammond, C., Feldman, W., McComas, D., Phillips, J., & Forsyth, R. 1996, A&A, 316, 350
Hefti, S., Zurbuchen, T. H., Fisk, L. A., et al. 1999, AIPC, 471, 495
Hellinger, P., Trávníček, P. M., Kasper, J. C., & Lazarus, A. J. 2006, Geophys. Res. Lett., 33, L09101
Holmes, J., Kasper, J. C., Klein, K., Lepri, S. T., & Raines, J. M. 2024, ApJ, 964, 19
Horaites, K., Boldyrev, S., Wilson, L. B. III, Viñas, A. F., & Merka, J. 2018, MNRAS, 474, 115
Horbury, T. S., O'Brien, H., Carrasco Blazquez, I. et al. 2020a, A&A, 642, A9
Horbury, T. S., Woolley, T., Laker, R., et al. 2020b, ApJS, 246, 45
Horbury, T. S., Bale, S. D., McManus, M. D., et al. 2023, Phys. Plasmas, 30, 082905
Iroshnikov, P. S. 1963, Astronomicheskii Zhurnal 40, 742
Isenberg, P. A., & Hollweg, J. V. 1983, J. Geophys. Res., 88, 3923
Jagarlamudi, V. K., Raouafi, N. E., Bourouaine, S., et al. 2023, ApJ, 950, L7
Johnson, E., Maruca, B. A., McManus, M., et al. 2023, ApJ, 950, 51
Johnson, E., Maruca, B. A., McManus, M., et al. 2024, Front. Astron. Space Sci. 10:1284913
Kasper, J. C., & Klein, K. G. 2019, ApJ, 877, L35
Kasper, J. C., Stevens, M. L., Lazarus, A. J., Steinberg, J. T., & Ogilvie, K. W. 2007, ApJ, 660, 901
Kasper, J. C., Lazarus, A. J., & Gary, S. P. 2008, Phys. Rev. Lett., 101, 261103
Kasper, J. C., Stevens, M. L., Korreck, K. E., et al. 2012, ApJ, 745, 162
Kasper, J. C., Maruca, B. A., Stevens, M. L., et al. 2013, Phys. Rev. Lett., 110, 091102
Kasper, J. C., Klein, K. G., Weber, T., et al. 2017, ApJ, 849, 126
Kiyani, K. H., Osman, K. T., & Chapman, S. C. 2015, Trans. R. Soc. A. 373, 20140155
Ko, Y.-K., Roberts, D. A., & Lepri, S. T. 2018, ApJ, 864, 139
Kolmogorov, A. N. 1941, Akademiia Nauk SSSR Doklady, 30, 301
Kraichnan, R. H. 1965, Phys. Fluids, 8, 1385
Landi, E., Gruesbeck, J. R., Lepri, S. T., et al. 2012, ApJ, 761, 48
Lavraud, B., & Larson, D. E. 2016, J. Geophys. Res., 121, 8462
Leamon, R. J., Smith, C. W., Ness, N. F., et al. 1998, J. Geophys. Res., 103, A3
Lepri, S. T., Landi, E., & Zurbuchen, T. H. 2013, ApJ, 768, 94
Lin R. P. 1997, Coronal Physics from Radio and Space Observations, ed. G. Trottet (Berlin: Springer), 483, 93
Lin R. P. 1998, Space Sci. Rev., 86, 61
Livi, S., Lepri, S. T., Raines, J. M., et al. 2023, A&A, 676, A36
Lopez, R. E., & Freeman, J. W. 1986, J. Geophys. Res., 91, 1701
López, R. A., Shaaban, S. M., Lazar, M., et al. 2019, ApJ, 882, L8
Louarn, P., Fedorov, A., Prech, L., et al. 2024, A&A, 682, A44
MacBride, B. T., Forman, M. A., & Smith, C. W. 2005, ESA SP, 592, 613
Macneil, A. R., Owens, M. J., Beri, L., & Finley, A. J. 2020, MNRAS, 498, 5273
Maksimovic, M., Pierrard, V., & Riley, P. 1997, Geophys. Res. Lett., 24, 1151
Maksimovic, M., Zouganelis, I., Chaufray, J.-Y., et al. 2005, J. Geophys. Res., 110, A09104
Marino, R., & Sorriso-Valvo, L. 2023, Phys. Rep., 1006, 1
Márquez Rodríguez, R., Sorriso-Valvo, L., & Yordanova, E. 2023, Sol. Phys., 298, 54
Marsch, E., & Livi, S. 1987, J. Geophys. Res., 92, 7263
Marsch, E., & Tu, C.-Y. 1990a, J. Geophys. Res., 95, 8211
Marsch, E., & Tu, C.-Y. 1990b, J. Geophys. Res., 95, 11945
Marsch, E., Rosenbauer, H., Schwenn, R., Muehlhaeuser, K. H., & Neubauer, F. M. 1982a, J. Geophys. Res., 87, 35
Marsch, E., Schwenn, R., Rosenbauer, H., et al. 1982b, J. Geophys. Res., 87, 52
Maruca, B. A., Kasper, J. C., & Gary, S. P. 2012, ApJ 748, 137

Maruca, B. A., Bale, S. D., Sorriso-Valvo, L., Kasper, J. C., & Stevens, M. L. 2013, Phys. Rev. Lett., 111, 241101
Maruca, B. A., Qudsi, R. A., Alterman, B. L., et al. 2023, A&A, 675, A196
Matteini, L., Landi, S., Hellinger, P. et al. 2007, Geophys. Res. Lett., 34, L20105
Matteini, L., Hellinger, P., Goldstein, B. E., et al. 2013, J. Geophys. Res., 118, 2771
Matteini, L., Horbury, T. S., Pantellini, F., Velli, M., & Schwartz, S. J. 2015, ApJ, 802, L11
Matteini, L., Stansby, D., Horbury, T. S., & Chen, C. H. K. 2018, ApJ, 869, L32
Matthaeus, W. H., & Goldstein M. L. 1986, Phys. Rev. Lett., 57, 495
Matthaeus, W. H., Elliott, H. A., & McComas, D. J. 2006, J. Geophys. Res., 111, A10103
McComas, D. J., Bame, S. J., Barracloug, B. L., et al. 1998, Geophys. Res. Lett., 25, 1
McComas, D. J., Goldstein, R., Gosling, J. T., & Skoug, R. M. 2001, Space Sci. Rev., 97, 99
McComas, D. J., Elliott, H. A., Schwadron, N. A., et al. 2003, Geophys. Res. Lett., 30, 1517
McManus, M. D., Bowen, T. A., Mallet, A., et al. 2020, ApJS, 246, 67
Mininni, P. D., & Pouquet, A. 2009, Phys. Rev. E, 80, 025401
Mondal, S., Banerjee, S., & Sorriso-Valvo, L. 2025, ApJ, 982, 199
Müller, D., St. Cyr, O. C., Zouganelis, I., et al. 2020, A&A, 642, A1
Neugebauer, M. 1976, J. Geophys. Res., 81, 78
Neugebauer, M., & Snyder, C. W. 1962, Science, 138, 1095
Neugebauer, M., & Snyder, C. W. 1966, J. Geophys. Res., 71, 4469
Neugebauer, M., Goldstein, B. E., Smith, E. J., & Feldman, W. C. 1996, J. Geophys. Res., 101, 17047
Nicolaou, G., Wicks, R. T., Owen, C. J., et. 2021, A&A, 656, A10
Noci, G., Kohl, J. L., Antonucci, E., et al. 1997, ESA SP, 404, 75
Ofman, L. 2000, Geophys. Res. Lett., 27, 2885
Owens, M. J., & Forsyth, R. J. 2013, Liv. Rev. Sol. Phys., 10, 5
Owens, M. J., Crooker, N. U., & Schwadron, N. A. 2008, J. Geophys. Res., 113, A11104
Owens, M. J., Lockwood, M., Riley, P., & Linker, J. 2017, J. Geophys. Res., 122, 10980
Owen, C. J., Bruno, R., Livi, S., et al. 2020, A&A 642, A16
Owen, C. J., Abraham, J.B., Nicolaou, G., et al. 2022, Universe, 8, 509
Panasenco, O., & Velli, M. 2013, AIP Conf. Proc., 1539, 50
Panasenco, O., Velli, M., & Panasenco, A. 2019, ApJ, 873, 25
Panasenco, O., Velli, M., D'Amicis, R., et al. 2020, ApJS, 246, 54
Perrone, D., D'Amicis, R., De Marco, R., et al. 2020, A&A, 633, A166
Pilipp, W. G., Miggenrieder, H., Montgomery, M. D., et al. 1987a, J. Geophys. Res., 92, 1075
Pilipp, W. G., Miggenrieder, H., Montgomery, M. D., et al. 1987b, J. Geophys. Res., 92, 1093
Podesta, J. J., Roberts, D. A., & Goldstein, M. L. 2006, J. Geophys. Res., 111, A10109
Podesta, J. J., Roberts, D. A., & Goldstein, M. L. 2007, ApJ, 664, 543
Politano, H., & Pouquet, A. 1998, Geophys. Res. Lett., 25, 273
Raouafi, N. E., Matteini, L., Squire, J., et al. 2023, Space Sci. Rev., 219, 8
Raymond, J. C., Kohl, J. L., Noci, G., et al. 1997, Sol. Phys., 175, 645
Richardson, J. D., Wang, C., &, Burlaga, L. F. 2004, Adv. Space Res., 34, 150
Rivera, Y. J., Badman, S. T., Stevens, M. L., et al. 2024a, Science, 385, 962
Rivera, Y. J., Badman, S. T., Stevens, M. L., et al. 2024b, ApJ, 974, 198
Rivera, Y. J., Badman, S. T., Verniero, J. L., et al. 2025a, ApJ, 980, 70
Rivera, Y. J., Klein, K. G., Wang, J. H., et al. 2025b, ApJ, 990, L60
Roberg-Clark, G. T., Drake, J. F., Swisdak, M., & Reynolds, C. S. 2018, ApJ, 867, 154
Roberts, D. A., Klein, L. W., Goldstein, M. L., & Matthaeus, W. H. 1987, J. Geophys. Res., 92, 11021
Roberts, D. A., Goldstein, M. L., Matthaeus, W. H., & Ghosh, S. 1992, J. Geophys. Res., 97, 17115
Roberts, D. A. 2010, J. Geophys. Res., 115, A12101
Saito, S., & Gary, S. P. 2007, J. Geophys. Res., 112, A4
Salem, C., Mangeney, A., Bale, S. D., & Veltri, P. 2009, ApJ, 702, 537
Salem, C., Pulupa, M., Bale, S. D., & Verscharen, D. 2023, A&A, 675, A162
Schrijver, C. J., & De Rosa, M. L. 2003, Sol. Phys., 212, 165
Schwenn, R. 2006, Space Sci. Rev., 124, 51
Schwenn, R., & Marsch, E. 1990, Physics of the Inner Heliosphere I, Large-Scale Phenomena (New York: Springer-Verlag Berlin Heidelberg)
Shearer, P., von Steiger, R., Raines, J. M., et al. 2014, ApJ, 789, 60
Shi, X., Fu, H., Yan, L., Lui, Q., & Xia, L., 2025, ApJS, 281, 2
Smith, E. J., Tsurutani, B. T., & Rosenberg, R. L. 1978, J. Geophys. Res., 83, 717
Smith, C. W., Stawarz, J. E., Vasquez, B. J., Forman, M. A., & MacBride, B. T. 2009, Phys. Rev. Lett., 103, 201101
Sorriso-Valvo, L., Carbone, V., Veltri, P., Consolini, G., & Bruno, R. 1999, Geophys. Res. Lett., 26, 1801
Sorriso-Valvo, L., Carbone, V., Veltri, P., Politano, H., & Pouquet, A. 2000, EPL, 51, 520
Sorriso-Valvo, L., Carbone, V., Noullez, A., et al. 2002, Phys. Plasmas, 9, 89
Sorriso-Valvo, L., Marino, R., Carbone, V., et al. 2007, Phys. Rev. Lett., 99, 115001
Sorriso-Valvo, L., Yordanova, E., Dimmock, A. P., & Telloni, D. 2021, ApJ, 919, L30
Sorriso-Valvo, L., Marino, R., Foldes, R., et al. 2023, A&A, 672, A13
Stakhiv, M., Landi, E., Lepri, S. T., Oran, R., & Zurbuchen, T. H. 2015, ApJ, 801, 100
Stansby, D., Horbury, T. S., & Matteini, L., 2018, MNRAS, 482, 1706
Stansby, D., Perrone, D., Matteini, L., Horbury, T. S., & Salem, C. S. 2019, A&A, 623, L2
Stansby, D., Matteini, L., Horbury, T. S, et al. 2020, MNRAS, 492, 39
Štverák, S., Trávníček, P., Maksimovic, M., et al. 2008, J. Geophys. Res., 113, A03103
Štverák, Š., Herčík, D., Nicolaou, G., et al. 2025, A&A, 693, A185
Tao, J., Wang, L., Zong, Q., et al. 2016, ApJ, 820, 22
Taylor, G. I. 1938, R. Soc. London Proc. Ser. A, 164, 476
Telloni, D., Bruno, R., & Trenchi, L. 2015, ApJ, 805, 46
Thepthong, P., Pongkitiwanichakul, P., Ruffolo, D., et al. 2024, ApJ, 962, 37
Thieme, K. M., Marsch, E., & Schwenn, R. 1987, Proceedings of the 6th International Solar Wind Conference (317–321). In V. J. Pizzo, T. Holzer, & D. G. Sime (Eds.,) Colorado: YMCA of the Rockies, Estes Park
Thieme, K. M., Schwenn, R., & Marsch, E. 1989, Adv. Space Res., 9, 127
Tracy, P. J., Kasper, J. C., Zurbuchen, T. H., et al. 2015, ApJ, 812, 170
Tracy, P. J., Kasper, J. C., Raines, J. M., et al. 2016, Phys. Rev. Lett., 116, 255101
Tu, C.-Y., & Marsch, E. 1991, Ann. Geophys., 9, 3192
Tu, C.-Y., & Marsch, E. 1993, J. Geophys. Res., 98, 1257
Tu, C. Y., & Marsch, E. 1995, Space Sci. Rev., 73, 1
Tu, C.-Y., Marsch, E., & Thieme, K. M. 1989, J. Geophys. Res., 94, 11739
Verdini, A., Grappin, R., Pinto, R., & Velli, M. 2012, ApJ, 750, L33
Verscharen, D, Klein, K. G., & Maruca, B. A. 2019a, Liv. Rev. Sol. Phys., 16, 5
Verscharen, D., Chandran, B. D. G., Jeong, S.-Y., et al. 2019b, ApJ, 886, 136
Vocks, C., Salem, C., Lin, R. P., & Mann, G. 2005, ApJ, 627, 540
von Steiger, R. 2008, in The Heliosphere Through the Solar Activity Cycle, eds. Balogh, A., Lanzerotti, L., & Suess, S. T., (Chichester, UK: Springer Praxis), Ch. 3, 41
von Steiger, R., & Zurbuchen, T. H. 2011, J. Geophys. Res., 116, A01105
von Steiger, R., Schwadron, N. A., Fisk, L. A., et al. 2000, J. Geophys. Res., 105, 27217
Wang, Y.-M. 1994, ApJ, 437, L67
Wang, Y.-M., & Sheeley, N. R. 1990, ApJ, 365, 372
Wang, Y.-M., Sheeley, N. R., Howard, R. A., Rich, N. B., & Lamy, P. L. 1999, Geophys. Res. Lett., 26, 1349
Wang, L., Lin, R. P., Salem, C., et al. 2012, ApJ, 753, L23
Woolley, T., Matteini, L., McManus, M. D., et al. 2021, MNRAS, 508, 236
Wu, H., Tu, C., He, J., Wang, X., & Yang, L. 2022, ApJ, 927, 113
Wu, H., Huang, S., He, J., et al. 2025, A&A, 697, A187
Wu, X., Owen, C. J, Coburn, J., et al. 2026, ApJ, 1000, 13
Xu, F., & Borovsky, J. E. 2015, J. Geophys. Res., 120, 70
Yang, L., Wang, L., He, J., et al. 2015, RAA, 15, 348
Yardley, S. L., Brooks, D. H., D'Amicis, R., et al. 2024, Nat. Astron., 8, 953
Yermolaev, Y. I., & Stupin, V. V. 1997, J. Geophys. Res., 102, 2125
Yogesh, C. D., & Srivastava, N. 2021, MNRAS, 503, L17
Zank, G. P., & Matthaeus, W. H. 1992, J. Geophys. Res., 97, 17189
Zank, G. P., Adhikari, L., Hunana, P., et al. 2017, ApJ, 835, 147
Zhao, L., Zurbuchen, T. H., & Fisk, L. A. 2009, Geophys. Res. Lett., 36, L14104
Zhao, L., Landi, E., Lepri, S. T., et al. 2017, ApJS, 228, 4
Zhao, L., Landi, E., Lepri, S. T., & Carpenter, D. 2022, Universe, 8, 8
Zurbuchen, T. H. 2007, Annu. Rev. Astron. Astrophys. 45, 297
Zurbuchen, T. H., Hefti, S., Fisk, L. A., Gloeckler, G., & von Steiger, R. 1999, Space Sci. Rev., 87, 353
Zurbuchen, T. H., Fisk, L. A., Gloeckler, G., & von Steiger, R. 2002, Geophys. Res. Lett., 29, 1352

Appendix A: Tools for studying turbulence

Elsässer variables are defined in the following way: $z^{\pm} = v \pm b$, where v and b are the velocity and magnetic fluctuating field where the average background filed as been substracted. In particular, b is the magnetic field vector in Alfvén units for a background magnetic field pointing toward the Sun, while $z^{\pm} = v \mp b$ for the opposite polarity. This definition allows to always identify z^{+} with outward propagation modes (with respect to the Sun) while z^{-} with inward modes (fluctuations).

In particular, we computed the three components of z^{+} and z^{-} in RTN and then the power spectral density of the trace of their components, $e^{\pm}$ versus f, that is the energy associated to these propagating modes, either inward or outward. We then derived the normalized cross-helicity in the frequency domain: $\sigma_C(f) = (e^{+}(f) - e^{-}(f))/(e^{+}(f) + e^{-}(f))$, that measures the predominance of z^{+} on z^{-} or vice-versa. σ_C equal to 1 (-1) indicates the presence of only the outward (inward) component, while $|\sigma_C| < 1$ corresponds to mixed inward and outward modes and/or non-Alfvénic fluctuations (Bruno & Carbone 2013).

The energy imbalance of the fluctuations in the spectral domain can be evaluated by computing first the trace of the power spectral density of velocity components (here indicated as $e^{V}(f)$), and b in Alfvén units, $e^{b}(f)$. The ratio between these two quantities corresponds to the Alfvén ratio. We then defined the normalized residual energy in the frequency domain, $\sigma_R(f) = (e^{V}(f) - e^{b}(f))/(e^{V}(f) + e^{b}(f))$. σ_R is linked to r_A by $(r_A - 1)/(r_A + 1)$. σ_R equal to +1 (−1) indicates the absence of magnetic (kinetic) fluctuations. Pure Alfvénic fluctuations are expected to show equipartition of energy: $\sigma_R = 0$ (or $r_A = 1$) (Tu & Marsch 1995).

Appendix B: Role of the different ion populations in the energy balance of solar wind fluctuations

In this section, we further investigated the tendency toward a kinetic energy imbalance observed in the fast wind (Figure 7) by exploiting the clustering technique originally introduced by De Marco et al. (2023) and subsequently developed by Bruno et al. (2024). This approach allows us to account for the contribution of alpha particles to the energetics of fluctuations (Bavassano & Bruno 2000). In particular, Bruno et al. (2024) analyzed the kinetic properties of protons and alpha particles, distinguishing between their core and beam populations, in the same fast stream considered in the present study. Here, we use the same dataset to assess the role of the different ion populations and to determine whether the observed energy imbalance has a physical origin.

Clustering applied to 3D VDFs observed by SWA-PAS allows to separate the full 3D VDF in four 3D VDFs (referred to proton core and beam, alpha core and beam) and then derives the moments (or bulk parameters) of distributions of the different ion species. Although Bruno et al. (2024) did not perform a spectral analysis, Figure 21 of their paper already gave an indication of a kinetic imbalance for the proton core since they found a slope in the scatter plot of V_N versus V_{AN} close to 1.5. In this sense, the balance of energy expected for ideal alfvénic fluctuations can be properly reached when all the populations are included in the calculations. This argument can explain the findings of Figure 7 of the present paper (fast wind, middle panel), where we show a σ_R slightly imbalanced toward positive values. By separating the population of the fast wind interval using the clustering technique, we performed the spectral analysis of σ_R by considering the velocity obtained from protons and alpha particles. In this case, the mass density used to define V_A takes into account also the contribution of both protons and alpha particles. Figure B.1 shows the comparison of the spectrum calculated by including the contribution of proton and alpha particles along with the σ_R spectrum obtained by using L2 data. From this figure, it is clear that accounting for all the contributions from the different solar wind populations is essential to correctly assess the energetics of fluctuations, in agreement with the model proposed by Bruno et al. (2024). Through the present spectral analysis, this concept is further elucidated in the frequency domain. In particular, while moments computed using proton-only measurements (L2 data) indicate a slightly positive energy imbalance, the inclusion of alpha particles in the calculation leads the residual energy back toward equipartition.

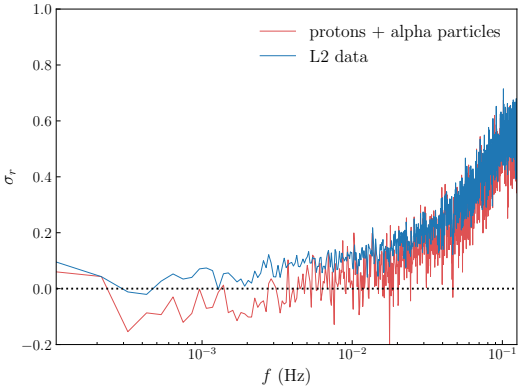


Fig. B.1. Comparison of the normalized residual energy, σ_R, in the frequency domain, for the fast wind, when considering the contribution of the different ion populations: protons + alpha particles (red) and L2 data (blue).